
CHAPTER 118

A Review of Strain Field Calculations in Embedded Quantum Dots and Wires

R. Maranganti, P. Sharma

University of Houston, Department of Mechanical Engineering, Houston, Texas, USA

CONTENTS

1.	Introduction	1
2.	Review of Strain Field Calculations in Quantum Dots and Wires	3
2.1.	Simple Illustrative Example	4
2.2.	Effect of Shape	6
2.3.	Effect of Presence of a Free Surface in Near Vicinity	20
2.4.	Effect of Material Anisotropy and Nonlinearity	23
2.5.	Effect of Coupled Fields: Piezoelectricity	27
2.6.	Effect of Size	30
2.7.	Some Results from Inclusion Theory Useful for Strain Calculations in Quantum Dot Structures	38
3.	Summary and Open Issues	39
	References	40

1. INTRODUCTION

Quantum dots (QDs) are tiny dimensionally confined (typically semiconductor) objects where quantum effects become obvious, for example, energy spectra become discrete (see Fig. 1). QDs are characterized by a sharp density of states (DOS) reminiscent of “atoms.” To be more precise, a semiconductor material cluster may be termed a quantum dot if its characteristic dimensions become comparable to the exciton Bohr radius. For example, in case of GaAs, the exciton Bohr radius is roughly 10 nm. They are of immense technological importance and (while several technological barriers remain) are often considered as basis for several revolutionary nanoelectronic devices and applications (Fig. 2), for example, next-generation lighting [1–2], lasers [3–4], quantum computing, information storage and quantum cryptography [5–7], biological labels [8], sensors [9] and many others [10–12, 18–20]. QDs and quantum wires (QWRs) are typically embedded in another material with differing

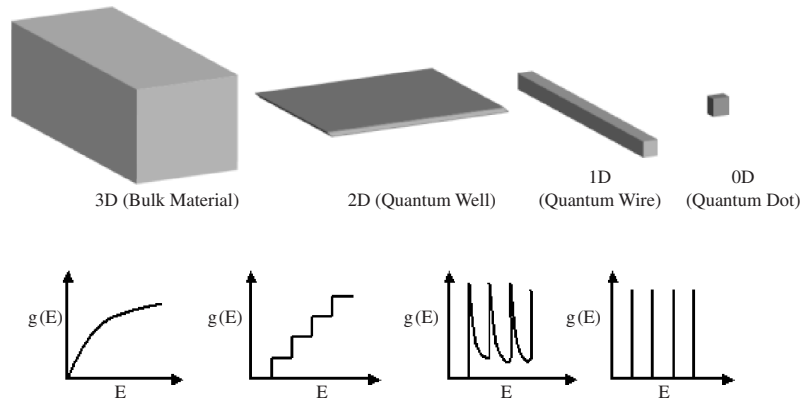


Figure 1. As the dimensionality of the structure reduce DOS, $g(E)$, becomes sharper and pronouncedly discrete.

elastic constants and lattice parameter. Because of the lattice mismatch, both the QD and host matrix strain and relax elastically to accommodate this mismatch and thus admit a state of stress (Fig. 3). As is well known, the electronic structure and the consequent optoelectronic properties of QDs are severely impacted due to this lattice mismatch induced strain [13–16]. In this article, we review pertinent literature on various methods to calculate the

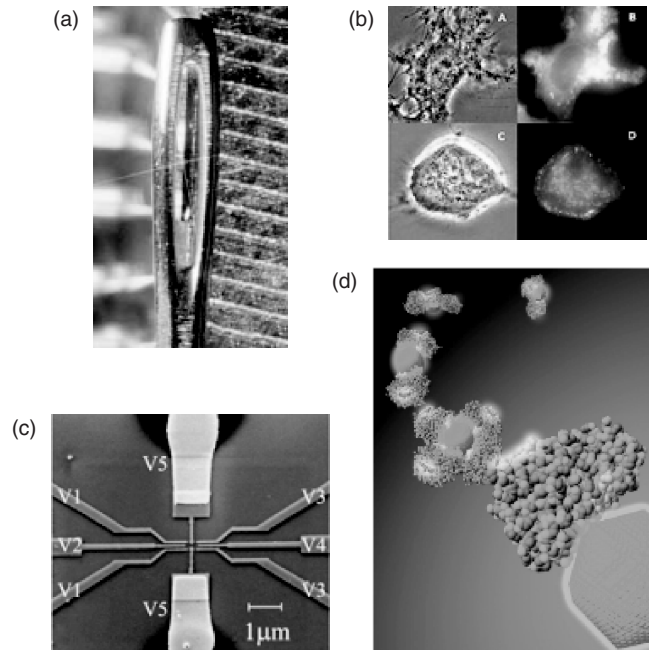


Figure 2. Different applications of quantum wires and dots. (a) Image of a quantum wire laser operating through the eye of a needle. Reproduced with permission from C. Jagadish, Research School of Physical Sciences and Engineering, Australian National University, © (2005). Increased recombination probability and discrete nature of DOS results in efficient lasing characteristics at low threshold currents along with the promise of tunable wavelength. (b) Magnified view of quantum dot attachment to neurons. Reproduced with permission from [18], Winter et al., *Adv. Mater.* 13, 1673 (2001). © 2001, Wiley VCH, Verlag GmbH & Co. Pictured here is the magnification of quantum dot attachment to neurons using antibody (A, B) and peptide (C, D) binding techniques. In B and D, the blue color is the self-fluorescence of the cell’s cytoplasm, and the yellow/orange color is the quantum dot luminescence. Using nanostructure sensors such as these, cellular-level target specificity at biological-electronic interfaces can be achieved as against conventional silicon-based electrodes where interfaces are at the tissue level. (c) Image of a quantum dot based transistor. Reproduced with permission from [19], Chen et al., *Phys. Rev. Lett.* 92, 176801 (2004). © 2004, American Physical Society. Transistors form vital switching components in computers. With quantum-dot based transistors as the one shown in the figure, “quantum computers,” can be realized. The memory of a quantum computer can simultaneously be both in “0” (off) and “1” (on) states (in general a superposition of these states) compared to a classical computer’s memory which is made up of either a “0” bit or a “1” bit. (d) Illustration of a quantum dot-based sensor for analyte detection. Reproduced with permission from [20], Medintz et al., *Nat. Mater.* 2, 630 (2003). © 2003, Nature Publishing Group.

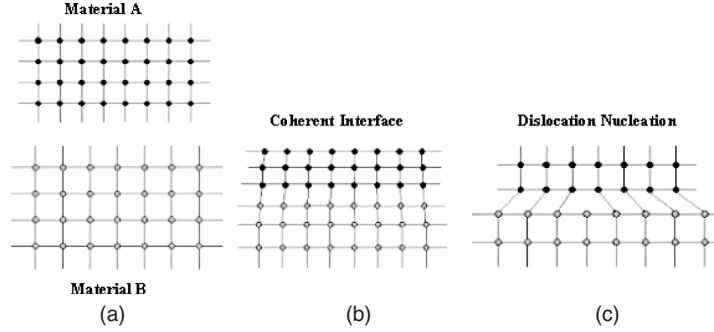


Figure 3. (a) Illustrates two materials “A” and “B” with different lattice constants; (b) formation of a “coherent” interface between A and B, requires that the lattice mismatch is completely accommodated by elastic deformation; (c) depicts the situation where the lattice mismatch is so high that further elastic deformation is energetically too costly and it is preferable to nucleate misfit dislocations. Such an interface is called a semicoherent interface.

state of strain in embedded *coherent* QDs and QWRs; That is, interface dislocations are absent. The impact of dislocations, if formed, on optoelectronic properties is so severe that an entirely different sort of discussion is required. In this review article, we mainly focus on the scenario when misfit dislocations are absent in the very near vicinity of the QD. This is indeed practical for small QDs [17].

The chapter is semitutorial in nature to make it accessible to readers from a broad range of disciplines. The rest of this chapter is organized in two broad sections. In Section 2, we provide, intermixed with a literature review, details on various methods and issues in calculation of strains in embedded QDs. Our particular focus is on cataloging the known analytical expressions. Physical insights obtained from both analytical results and numerical simulations of various researchers (including our own) are also discussed. The effect of various parameters such as material anisotropy, QD shape, surface image forces, elastic nonlinearity and piezoelectricity are addressed (Section 2.2–2.6). Typically classical continuum mechanics, which is intrinsically size independent, is employed for strain calculations. To address this, we have also included a brief discussion on the effect of QD size on strain calculations since most QD are in the sub-20-nm range, and one indeed expects a departure from classical mechanics at such small sizes (Section 2.7). In Section 2.8, we briefly review some relevant results in the elastic theory of inclusions, which while well known in the solid mechanics community, may be less known in the QD literature and are thus likely to be useful to engineers and scientists working in the latter research area. We conclude with a summary in Section 3 where we also present a rather terse personal viewpoint on some future research avenues in this research topic.

2. REVIEW OF STRAIN FIELD CALCULATIONS IN QUANTUM DOTS AND WIRES

QDs occur or are fabricated in a variety of shapes, sizes, and material combinations. Classical continuum elasticity (and less frequently, atomistic methods) are typically employed to calculate the strains in these structures, which are then linked to suitable band structure calculation methods to estimate the strained optoelectronic behavior. A review of band structure calculation methods for strained quantum structures is beyond the scope of the present article and the reader is referred to some excellent resources in the literature [12, 21–22].

Classical linear elastostatics is governed by the following set of partial differential equations (Eq. [1]) along with appropriate boundary conditions at the interfaces/surfaces (Eq. [2]):

$$\boldsymbol{\varepsilon} = \frac{1}{2}[(\nabla \otimes \mathbf{u})^T + (\nabla \otimes \mathbf{u})] \quad (1a)$$

$$\mathbf{div} \boldsymbol{\sigma} + \mathbf{f} = 0 \quad (1b)$$

$$\boldsymbol{\sigma} = \mathbf{C} : (\boldsymbol{\varepsilon} - \boldsymbol{\varepsilon}^m) \quad (1c)$$

Equation (1a) relates the second-order strain tensor ($\boldsymbol{\varepsilon}$) to the displacement vector (\mathbf{u}). ∇ is the gradient operator and superscript “ T ” indicates transpose operation. Equation (1b) written in terms of the second-order stress tensor ($\boldsymbol{\sigma}$) is the equilibrium equation with external body forces (\mathbf{f}) while Eq. (1c) relates the stresses and strain (note that $\boldsymbol{\varepsilon}^m$ is the lattice-mismatch strain) through a fourth-order elasticity tensor (\mathbf{C}). We shall use both bold-face and index notation as convenient. Unless noted otherwise, all tensors are Cartesian and conventional summation rules for repeated indices apply. Boundary condition can be either prescribed tractions or displacements. In the context of embedded QD/QWRs (typically), the following conditions at the interfaces and free surfaces are obeyed:

$$[\boldsymbol{\sigma}]\mathbf{n} = \mathbf{0}; \quad [\mathbf{u}] = \mathbf{0} \quad (2)$$

The vector \mathbf{n} is the normal at a point on the interface. The symbol $[\bullet]$ denotes jump in the field quantities across an interface. In particular for free surface, the traction-free condition $\boldsymbol{\sigma} \cdot \mathbf{n} = \mathbf{0}$ is satisfied.

Considering the easy and economic availability of commercial numerical packages (e.g., finite element tools) that can solve Eq. (1) for arbitrary geometry, material symmetry, and boundary conditions, discussion of analytical solutions may seem somewhat redundant and antiquated. However, much effort has been expended to develop such analytical models that have proved to be extremely useful in obtaining explicit physical insights and often, reasonable accuracy. Further, one must note that eventually, the strain calculations must be coupled to quantum mechanical equations for band structure calculations, which often proceeds numerically. Analytical expressions for strain can significantly simplify that process. In Section 2.1, we provide a simple illustrative example for calculation of strain in the idealized case of a deeply buried, embedded spherical quantum dot.

2.1. Simple Illustrative Example

Consider a spherical quantum dot (Ω) of radius R (Fig. 4), located in an infinite amount of host material (\mathbf{D}). The assumption of infinite host medium corresponds to the situation where the QD is deeply buried and the host matrix boundaries do not impact its strain state. In other words, the distance of the QD from any free boundary is significantly larger than the QD radius (typically $> 3R$).

Let the lattice parameter of the QD be a_{QD} and that of the matrix be a_M . The lattice mismatch strain tensor is then:

$$\boldsymbol{\varepsilon}_{ij}^m = \boldsymbol{\varepsilon}^m \delta_{ij}; \quad \boldsymbol{\varepsilon}^m = \frac{a_{\text{QD}} - a_M}{a_M} \quad (3)$$

Some authors choose to divide $a_{\text{QD}} - a_M$ by the average of the two lattice parameters. We assume for the purpose of this simple example that the material properties of both QD and matrix are isotropic; that is, the elastic tensor can be expressed in terms of the two Lamé constants (λ, μ):

$$C_{ijkl} = \lambda \delta_{ij} \delta_{kl} + \mu (\delta_{ik} \delta_{jl} + \delta_{il} \delta_{jk}) \quad (4)$$

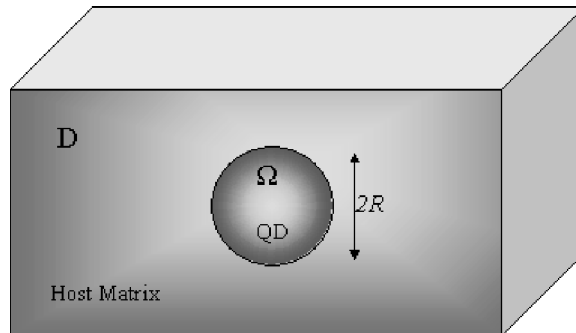


Figure 4. Schematic of the spherical quantum dot (Ω) embedded in an infinite host matrix (\mathbf{D}).

In this simple example, it is easier to work in terms of displacement. Equations (1) can be rewritten in terms of displacement (Navier's equations):

$$\mu \nabla^2 \mathbf{u} + \frac{\mu}{1-2\nu} \operatorname{div} \operatorname{grad} \mathbf{u} + \mathbf{f} = \mathbf{0} \quad (5)$$

Here, ν , is the Poisson ratio. To calculate stress, any nonelastic contribution (such as the mismatch strain) must be subtracted from the actual strain before employing Hooke's law. That is, for isotropic materials, the constitutive law in Eq. (1) can be rewritten as

$$\boldsymbol{\sigma} = \lambda_{\text{QD}} (\operatorname{Tr} \boldsymbol{\varepsilon} - \operatorname{Tr} \boldsymbol{\varepsilon}^m) \mathbf{I} + 2\mu_{\text{QD}} (\boldsymbol{\varepsilon} - \boldsymbol{\varepsilon}^m) \quad (6)$$

Here \mathbf{I} is the identity tensor. No subtraction of the mismatch strain is necessary when calculating the matrix stresses since (according to convention we adopted in Eq. (3), the mismatch strain is calculated with respect to zero reference strain in the matrix.

The problem under consideration with all its attendant assumptions is manifestly spherically symmetric and hence must admit a displacement field that is purely radial, that is, $\mathbf{u} = u(r)\mathbf{e}_r$. The corresponding infinitesimal strain tensor in spherical polar basis ($\mathbf{e}_r, \mathbf{e}_\theta, \mathbf{e}_\phi$) can be written as

$$\boldsymbol{\varepsilon} = \frac{\partial u}{\partial r} \mathbf{e}_r \otimes \mathbf{e}_r + \frac{u}{r} \mathbf{e}_\theta \otimes \mathbf{e}_\theta + \frac{u}{r} \mathbf{e}_\phi \otimes \mathbf{e}_\phi \quad (7)$$

Equation (5) or the Navier's equation then reduces to

$$\frac{\partial^2 u}{\partial r^2} + \frac{2}{r} \frac{\partial u}{\partial r} - \frac{2u}{r^2} = 0 \quad (8)$$

The general solutions to the differential equation of Eq. (8) are simply, r and $1/r^2$, that is,

$$u(r) = Ar + Br^{-2} | r < R \quad (9a)$$

$$Cr + Dr^{-2} | r > R \quad (9b)$$

Here, $A, B, C,$ and D are constants to be determined from the boundary conditions. Two boundary conditions are immediately obvious: (1) since the problem is a purely dilatational problem with spherical symmetry, at the center of the quantum dot $u(r)$ must approach zero and (2) at points infinitely far away from the quantum dot, the displacement must decay to zero. These restrictions render $B = C = 0$. Further, as per the boundary conditions in Eq. (2), the displacements must be continuous, thus $u^+(r \rightarrow R) = u^-(r \rightarrow R)$, while the traction continuity condition ensures that $\sigma_{rr}^+ - \sigma_{rr}^- = 0$. The final solution is obtained as

$$u(r) = \begin{cases} \frac{3K_{\text{QD}}\varepsilon^m}{4\mu_M + 3K_{\text{QD}}} r; & r \leq R \\ \frac{3K_{\text{QD}}\varepsilon^m}{4\mu_M + 3K_{\text{QD}}} \frac{R^3}{r^2}; & r > R \end{cases} \quad (10a)$$

$$\quad (10b)$$

Here the subscript M refers to matrix properties. Strain components and in particular the dilation (which has the dominant effect in electronic calculations) can be trivially obtained to be

$$\varepsilon_{rr}(r) = \varepsilon_{\theta\theta}(r) = \varepsilon_{\phi\phi}(r) = \frac{3K_{\text{QD}}\varepsilon^m}{3K_{\text{QD}} + 4\mu_M} \Big|_{r < R} \quad (11a)$$

$$\varepsilon_{rr}(r) = \left[\frac{3K_{\text{QD}}\varepsilon^m}{3K_{\text{QD}} + 4\mu_M} \right] \frac{R^3}{r^3} \Big|_{r > R} \quad (11b)$$

$$\varepsilon_{\theta\theta} = \varepsilon_{\phi\phi}(r) = - \left[\frac{3K_{\text{QD}}\varepsilon^m}{3K_{\text{QD}} + 4\mu_M} \right] \frac{R^3}{2r^3} \Big|_{r > R} \quad (11c)$$

Yang et al. [23] performed similar analytical calculations on $\text{Si}_{0.8}\text{Ge}_{0.2}$ sphere, cylinder and a rectangular slab embedded in an infinite Si host and linked these results to band-structure calculations. Numerical results were also obtained for V-groove $\text{Si}_{0.8}\text{Ge}_{0.2}$ quantum wires under anisotropy considerations [23].

An important point to note is that for band-gap calculations, *the mismatch strain is subtracted from the actual compatible elastic strain*. As a result while in the solid mechanics community the compatible elastic strain is normally expressed and plotted (as we have done so in Fig. 5), the QD research community often illustrate the subtracted strain (see, e.g., Yang et al. [23]). This can potentially cause confusion and care must be exercised in interpreting results from the solid mechanics literature. The simple idealized example in Fig. 5 illustrates and underscores several rather general features: (1) the strain state is uniform inside the quantum dot—as shall be seen, this is a general feature for all ellipsoidal shaped quantum dots; (2) the dilation too is uniform inside the QD; we emphasize this trivial point here since, as will be discussed in the next section, the dilation is uniform for *all quantum dot shapes* (provided certain assumptions such as unbounded host material, etc., are not violated); (iii) the dilation is zero outside the QD. This also is true for *all QD shapes*.

2.2. Effect of Shape

Some of the commonly occurring configurations of quantum dots and wires are illustrated in Fig. 6.

The reader is referred to these references [24–29] that report evidence of a wide variety of shapes, including pyramidal, truncated pyramidal, lens shaped, hemispherical, multifaceted domes, and so on, for the widely studied $\text{In}_x\text{Ga}_{1-x}\text{As}/\text{InAs}$ quantum dot system. Owing to the inherent size independence of classical continuum elasticity, strain state calculations depend exclusively on inclusion shape—to be more precise, self-similar structures if scaled larger or smaller yield identical results for strains and stresses.

Several of the methodologies that emerged in the context of QD/QWR strain calculations can be considered to be off-shoots or modifications of the now classical work of Eshelby

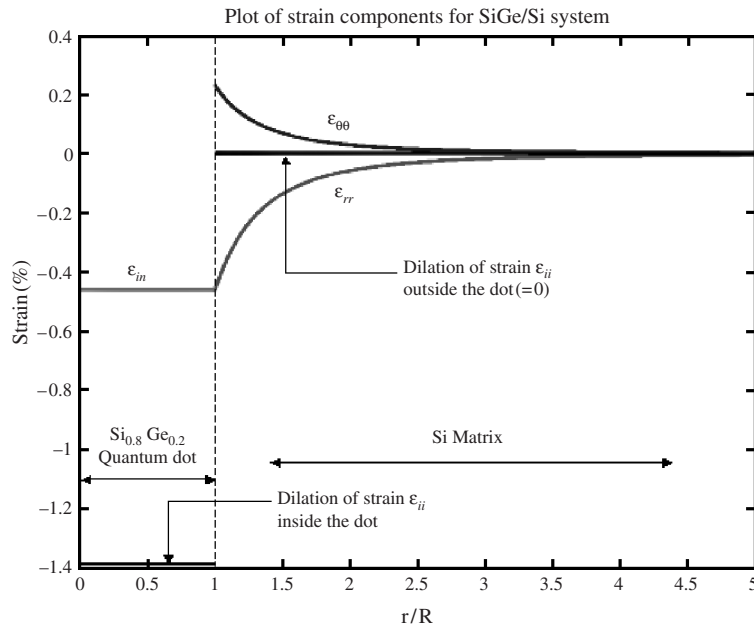


Figure 5. Plot of the strain components for a $\text{Si}_{0.8}\text{Ge}_{0.2}$ spherical quantum dot embedded in an infinite Si matrix versus the ratio (r/R). Uniform strain ϵ_{in} exists inside the quantum dot. Outside the dot, $\epsilon_{\theta\theta}$ is one of the tangential components of strain and ϵ_{rr} is the radial component of strain. As is noticeable, the dilation of strain ϵ_{ii} outside the dot is zero. One can notice the rapid decay of the strain outside the dot to a zero value at values of r/R as low as 3.5.

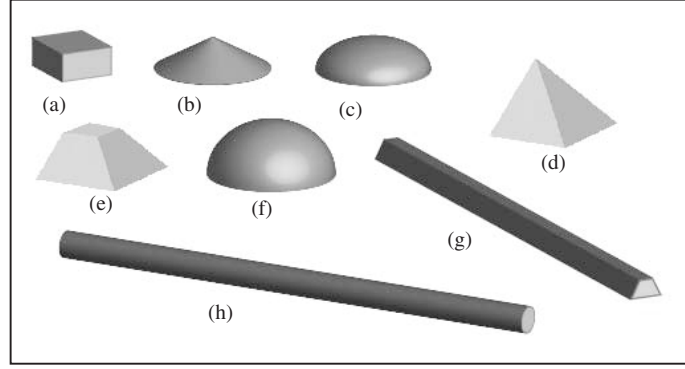


Figure 6. Common configurations of QDs and QWRs. (a) Cuboidal, (b) conical, (c) lens shaped, (d) pyramidal, (e) truncated pyramidal, (f) hemispherical, (g) trapezoidal QWR, (h) cylindrical QWR.

[30–32] on inclusions and inhomogenities. His elegant formalism provides rather straightforward means to evaluate the effect of shape for, in principle, arbitrary shaped quantum dots and wires. We first discuss his formalism briefly before reviewing the specific literature on QD/QWRs. In addition to providing a historical setting, Eshelby’s work provides an excellent perspective on inclusion problems and more specifically, then the related works on QD/QWRs can be discussed in appropriate context. This discussion will greatly facilitate our presentation (Section 2.8) of some results on the theory of inclusions (based on Eshelby’s approach) that though widely known in the micromechanics community, do not appear to have been fully exploited in the context of quantum dots and wires.

2.2.1. Eshelby’s General Formalism for Shape Effects

Consider an arbitrary shaped inclusion (quantum dot) embedded in an unbounded material (the impact of finiteness of the surrounding material will be discussed in Section 2.3). Let a stress-free uniform transformation strain be prescribed within the domain of the QD (Figure 7). Lattice mismatch induced strain is an example of such a stress free transformation strain and so are, for example, thermal expansion mismatch strains, phase transformation strains among others. For the moment, we assume identical material properties for the QD and the matrix.

Although Eshelby’s general approach is not restricted to isotropic materials, analytical results are generally not tractable in the fully anisotropic case. Issues related to anisotropy are fully discussed in Section 2.4.1. For now, we assume isotropic elastic behavior. By definition, the transformation strain is only nonzero within the QD domain ($\mathbf{x} \in \Omega$), and thus we can write the constitutive law for the QD-matrix as follows:

$$\sigma_{ij} = 2\mu(\varepsilon_{ij} - \varepsilon_{ij}^m H) + \lambda\delta_{ij}(\varepsilon_{ll} - \varepsilon_{ll}^m H) \quad (12)$$

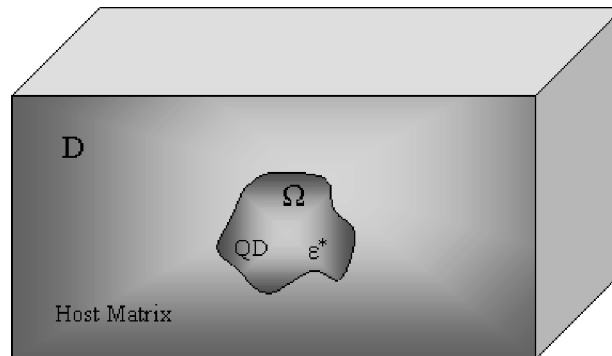


Figure 7. A quantum dot of arbitrary shape (Ω) inside an infinite matrix (D).

Here ‘‘H’’ is the step function defined as $H(\mathbf{x}) = \begin{cases} 1 & \mathbf{x} \in \Omega \\ 0 & \mathbf{x} \notin \Omega \end{cases}$. We can, analogous to Eq. (5), rewrite a Navier’s type equation:

$$\mu u_{i, ll} + (\mu + \lambda) u_{l, li} = -[(\lambda \varepsilon_{ll}^m \delta_{ik} + 2\mu \varepsilon_{ik}^m) H(\mathbf{x})]_{,k} \quad (13)$$

Clearly, the divergence of the mismatch strain $\varepsilon_{ik} H(\mathbf{x})$ defined over the inclusion volume act as delta functions across the inclusion surface i.e., $\varepsilon_{ik}^m \delta(S)$ (e.g., Refs. [30, 33]). A comparison with the Navier’s Eq. 5 indicates that the mismatch strain terms can be simulated as body forces. The displacement vector can be obtained using the Green’s function (of Eq. 5 or 13) as

$$\begin{aligned} u_i(\mathbf{x}) &= (\lambda \varepsilon_{ll}^m \delta_{jk} + 2\mu \varepsilon_{jk}^m) \int_S G_{ij}(\mathbf{x} - \mathbf{x}') dS_k(\mathbf{x}') \\ &= -(\lambda \varepsilon_{ll}^m \delta_{jk} + 2\mu \varepsilon_{jk}^m) \int_V G_{ij,k}(\mathbf{x} - \mathbf{x}') dV(\mathbf{x}') \end{aligned} \quad (14)$$

Here Gauss theorem has been used to convert the surface integral into a volume integral. The Green’s function for Navier’s equation is available in most books on elasticity (e.g., Ref. [34]) and can be written as

$$\begin{aligned} G_{ij}(\mathbf{r}) &= \frac{1}{8\pi(\lambda + 2\mu)} \left[(\lambda + 3\mu) \frac{\delta_{ij}}{|\mathbf{r}|} + (\lambda + \mu) \frac{x_i x_j}{|\mathbf{r}|^3} \right] \\ \mathbf{r} &= \mathbf{x} - \mathbf{x}'; \quad r = |\mathbf{r}| \end{aligned} \quad (15)$$

Upon substituting the Green’s function in Eq. (14) and invoking the strain-displacement law, we readily obtain [30]:

$$\varepsilon_{ij}(x) = \frac{1}{8\pi(1-\nu)} [\psi_{kl,klj} - 2\nu \phi_{kk,ij} - 2(1-\nu)(\phi_{ik,kj} + \phi_{jk,kl})] \quad (16)$$

where ψ and ϕ are biharmonic and harmonic potentials of the inclusion shape (Ω). They are given as:

$$\psi_{ij}(\mathbf{x}) = \psi \varepsilon_{ij}^m = \varepsilon_{ij}^m \int_\omega |\mathbf{x} - \mathbf{x}'| d^3 \mathbf{x}' \quad (17)$$

$$\phi_{ij}(\mathbf{x}) = \phi \varepsilon_{ij}^m = \varepsilon_{ij}^m \int_\omega \frac{1}{|\mathbf{x} - \mathbf{x}'|} d^3 \mathbf{x}' \quad (18)$$

Equation (16) is usually cast in the following form:

$$\begin{aligned} \boldsymbol{\varepsilon}(\mathbf{x}) &= \mathbf{S}(\mathbf{X}): \boldsymbol{\varepsilon}^m \quad \mathbf{x} \in \Omega \\ \boldsymbol{\varepsilon}(\mathbf{x}) &= \mathbf{D}(\mathbf{x}): \boldsymbol{\varepsilon}^m \quad \mathbf{x} \notin \Omega \end{aligned} \quad (19)$$

Here \mathbf{S} and \mathbf{D} are the so-called Eshelby tensors for interior and exterior points, respectively:

$$\{\mathcal{S}_{ijkl}, \mathcal{D}_{ijkl}\} = \frac{1}{8\pi(1-\nu)} \{\psi_{klj} - 2\nu \delta_{kl} \phi_{ij} - (1-\nu)[\phi_{kj} \delta_{il} + \phi_{ki} \delta_{jl} + \phi_{lj} \delta_{ik} + \phi_{li} \delta_{jk}]\} \quad (20)$$

One obtains \mathbf{S} or \mathbf{D} depending upon whether the vector \mathbf{x} in Eqs. (17 and 18) is located within the quantum dot or outside it. Eshelby’s tensors for various shapes (spheres, cylinders, ellipsoids, discs, and cuboids) are well documented in Mura [35]. For example, in the case of a spherical inclusion or quantum dot, we have

$$\psi(x) = \begin{cases} -\frac{1}{60}(r^4 - 10R^2 r^2 - 15R^4) & r \in \Omega \\ \frac{R^3}{15} \left(5r + \frac{R^2}{r} \right) & r \notin \Omega \end{cases} \quad (21)$$

$$\phi(x) = \begin{cases} -\frac{1}{6}(r^2 - 3R^2) & r \in \Omega \\ \frac{R^3}{3r} & r \notin \Omega \end{cases} \quad (22)$$

Using Eqs. (20)–(22) Eshelby's interior tensor can be then written explicitly as [35]

$$S_{ijkl} = \frac{5\nu - 1}{15(1 - \nu)} \delta_{ij} \delta_{kl} + \frac{4 - 5\nu}{15(1 - \nu)} (\delta_{ik} \delta_{jl} + \delta_{il} \delta_{jk}) \quad (23)$$

Here, ν is the Poisson ratio. The reader can trivially verify that use of Eshelby tensor expression above for strain calculation in a spherical quantum dot leads to the same results derived in a different way in Eq. (11) of Section 2.2 (provided the matrix properties are set to be the same as those of the quantum dot).

The implications of Eshelby's formalism are manifest. An evaluation of the harmonic and biharmonic potentials (Eqs. [17] and [18]) for various shapes, in principle, allows calculation of Eshelby's tensor and hence the complete strain state inside and outside the embedded quantum dot. An interesting outcome of Eshelby's analysis [30] is that for inclusions of ellipsoidal shape, \mathbf{S} is uniform. This implies that any quantum dot belonging to the ellipsoidal family immersed in an unbounded matrix subject to a uniform mismatch strain will admit a uniform strain! This is rather useful since the ellipsoidal shape is very versatile and can be used to mimic and approximate a variety of shapes (see Fig. 8). For the simple case of a spherical quantum dot, this fact has already been noted in the context of Eq. (11) and Fig. 5. This notion remains true even in the case of arbitrary anisotropy. This uniformity of strain rule does not in general hold true for nonellipsoidal shapes (e.g., polyhedral, pyramidal), in absence of linearity or if the matrix is not unbounded. As Eshelby [30] has pointed out, the peculiar property that ellipsoidal inclusions admit a uniform strain state under certain conditions is also very useful for taking into account the mismatch between the elastic moduli of the quantum dot and the surrounding matrix.

If only the dilatation is of interest, matters simplify considerably and we obtain:

$$Tr(\boldsymbol{\varepsilon}) = -\frac{9K\varepsilon^m}{4\mu + 3K} \nabla^2 \phi \quad (24)$$

Thus only the harmonic potential needs to be evaluated. Further, the general properties of the harmonic potential [30, 36–37] ensure that the dilation inside the quantum dot is *shape independent!* Again caution must be exercised in using this notion when, for example, the surrounding medium is not unbounded. Within the strict assumptions of the derivation

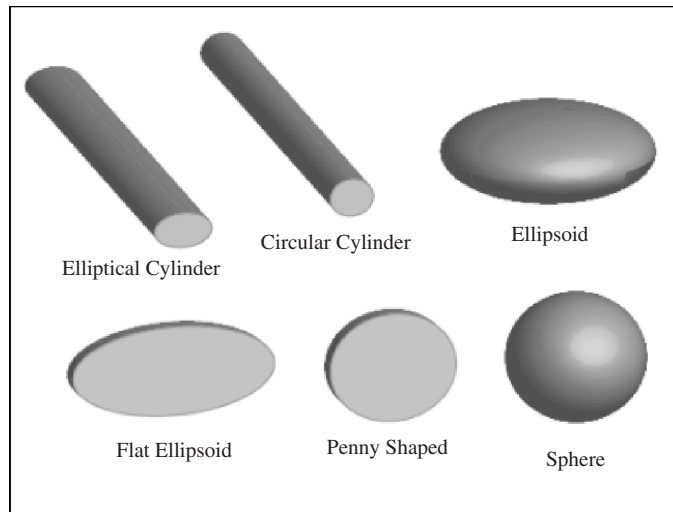


Figure 8. An illustration of the variety of shapes, which fall under the gamut of the general ellipsoid.

given by Eshelby [30] and partly reproduced here, this rather interesting fact suggests that in an isotropic unbounded medium, shape effects are of secondary importance insofar as *dilation* is concerned.

Since the strain state within the inclusion is uniform for ellipsoids, Eshelby [30] was able to devise an elegant method to mimic an inhomogeneity, that is, an inclusion with a mismatch strain and material properties differing from the host matrix, by an inclusion containing a fictitious transformation strain. Mura [35] defines an inclusion to be a subdomain in which a stress-free strain is prescribed but the material properties are same everywhere. An inhomogeneity is defined as an inclusion that has differing material properties from those of the surrounding matrix. The so-called equivalent inclusion method simply entails equating the elastic state of an inhomogeneity to that of an inclusion albeit with the aforementioned fictitious transformation strain that is,

$$\left. \begin{aligned} \mathbf{C}^M: \{\boldsymbol{\varepsilon} - \boldsymbol{\varepsilon}^m - \boldsymbol{\varepsilon}^f\} &= \mathbf{C}^H: \{\boldsymbol{\varepsilon} - \boldsymbol{\varepsilon}^m\} \\ \boldsymbol{\varepsilon} &= \mathbf{S}: \{\boldsymbol{\varepsilon}^m + \boldsymbol{\varepsilon}^f\} \end{aligned} \right\} \mathbf{x} \in \Omega \quad (25a)$$

$$(25b)$$

Equations (25) are simply algebraic equations that allow explicit determination of the fictitious transformation strain and hence the elastic moduli mismatch in the case of ellipsoidal quantum dots. For more general shapes, Eshelby's tensor is no longer uniform and hence these equations become rather complicated integral equations. This is will be further discussed when we address arbitrary shaped QDs in the next section.

2.2.2. Quantum Dots

In the specific context of QDs, fair amount of effort has been expended on general solutions (for example, see [38–44]). Some of the earlier works in regards to quantum dots strain calculations are due to Grundmann et al. [48] (see also Refs. [45–47]). They presented some simple analytical results for shapes such as slabs, circular cylinder and spherical. One notes that these results can, of course, also be recovered from Eshelby's formalism discussed in the previous section. For the specific case of InAs pyramidal-shaped quantum dots embedded in a GaAs matrix, Grundmann et al. [48] presented numerical simulations for the strain distributions. This shape is of course a bit difficult to handle analytically although closed-form solution can indeed be derived as will be discussed shortly. Although it is beyond the scope of the present article, their computation of the strain-linked electronic properties of InAs QDs is also of interest and they succeed in obtaining reasonable agreement with experimental data on luminescence and absorption.

Downes et al. [49] devised a simple method for calculating the strain distribution in deeply buried QD structures. Six vectors \mathbf{A}_{ij} are defined such that $\nabla \mathbf{A}$ yields the stress components $\boldsymbol{\sigma}_{\text{sph}}$ for a point spherical inclusion:

$$\mathbf{A}_{xx} = Dx \mathbf{i}; \quad \mathbf{A}_{xz} = -Dx \mathbf{k}; \quad \mathbf{A}_{xy} = -Dx \mathbf{i} \quad (26a)$$

$$\mathbf{A}_{yy} = Dy \mathbf{j}; \quad \mathbf{A}_{yz} = -Dz \mathbf{j}; \quad \mathbf{A}_{zz} = Dz \mathbf{k} \quad (26b)$$

$$D = \frac{\Lambda}{(x^2 + y^2 + z^2)^{3/2}}; \quad \Lambda = \frac{E \boldsymbol{\varepsilon}^m}{4\pi(1 - \nu)} \quad (26c)$$

Here, E is the Young's modulus. The stress tensor for a given QD shape can then be written as

$$\boldsymbol{\sigma}(\mathbf{x}) = \int_V \nabla \cdot \mathbf{A}(\mathbf{x} - \mathbf{x}') dV(\mathbf{x}') \quad (27)$$

Divergence theorem can then be invoked to convert the volume integral in Eq. 27 to a surface integral to obtain the strain field in and around an arbitrarily shaped QD.

$$\boldsymbol{\sigma}(\mathbf{x}) = \int_S \mathbf{A}(\mathbf{x} - \mathbf{x}') \cdot d\mathbf{S}(\mathbf{x}') \quad (28)$$

The QD surface may be discretized appropriately to convert the surface integral into a summation. This approach facilitates analytic solutions in the case of simple structures like

cuboidal QDs. Formally, this approach by Downes et al. [49] can be related to computing Eshelby's tensor. As example, the stress state of a parallelepiped dot can be easily related to its geometry, that is, lengths and the angles. For such a parallelepiped dot, centered on the origin and aligned along the Cartesian axes, with dimensions, $2a \times 2b \times 2c$, Eq. (28) provides the following stress components [60]:

$$\sigma_{xx} = \sum -\Lambda \tan^{-1} \left(\frac{(b \pm y)(c \pm z)}{(a \pm x) \sqrt{(a \pm x)^2 + (b \pm y)^2 + (c \pm z)^2}} \right) \quad (29a)$$

$$\sigma_{xz} = \sum q\Lambda \log \left\{ \sqrt{(x \pm a)^2 + (y \pm b)^2 + (z \pm c)^2} - (y \pm b) \right\} \quad (29b)$$

Here the summation is over the various combinations of + and -. In Eq. (28b), q is +1 for one or 3 plus signs and -1 for 0 or 2 plus signs. Identical results can be obtained using Eshelby's approach and indeed have been derived by Chiu [50] and are also documented in Mura [35]. When the dimension of the parallelepiped along one direction is very large compared with the other two dimensions, it degenerates to the case of a rectangular QWR and the results for the buried strained layer, both of which will be discussed later in this section. As noted by Downes et al. [49], the integral that is used to evaluate σ_{xx} is similar to the integral for the solid angle subtended by the two (100) faces of a parallelepiped aligned along the Cartesian axes (see Fig. 9). The hydrostatic stress inside such a dot ($\sigma_{xx} + \sigma_{yy} + \sigma_{zz}$) is thereby proportional to the solid angle subtended at an interior field point by all the faces of the cube (4π). This fact automatically ensures the constancy of the dilation within the dot. The solid angle is zero for an outside point and so is the hydrostatic strain.

One of the more common shapes for self-assembled quantum dots is the pyramidal geometry (Fig. 10). Finite-element methods have been employed to treat the strain distribution problem for pyramidal quantum dots [48, 51]. However, analytical solutions (although somewhat tedious) can also be readily obtained.

A generic point, (x_1^0, x_2^0, x_3^0) inside the volume of the pyramidal dot illustrated in Fig. 10 can be mathematically represented by

$$-a \left(1 - \frac{x_3^0}{h} \right) \leq x_1^0 \leq a \left(1 - \frac{x_3^0}{h} \right) \quad (30a)$$

$$-b \left(1 - \frac{x_3^0}{h} \right) \leq x_2^0 \leq b \left(1 - \frac{x_3^0}{h} \right) \quad (30b)$$

$$0 \leq x_3^0 \leq hf \quad (30c)$$

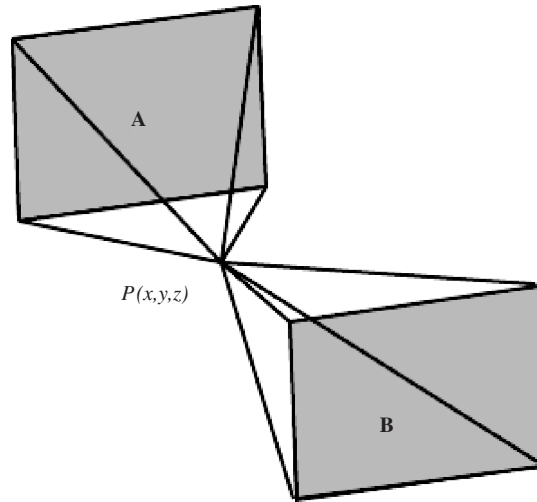


Figure 9. Illustration of the solid angle subtended at point $P(x, y, z)$ by two opposing faces, "A" and "B" of a cuboid. Adapted from Downes et al. [49].

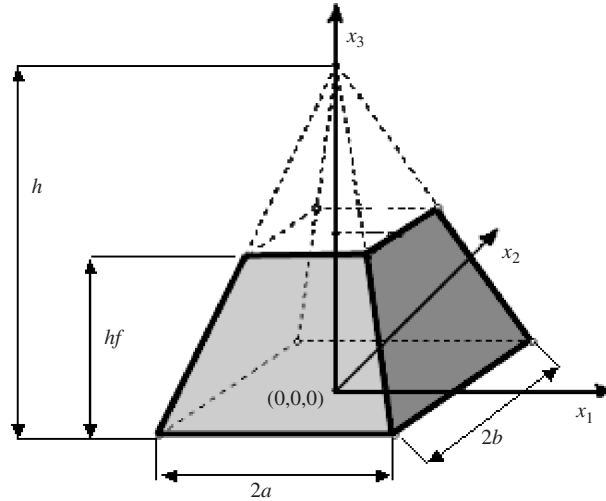


Figure 10. The geometry of the pyramidal quantum dot considered by Pearson and Faux [52] is illustrated; “ f ” represents the degree of truncation of the pyramid. Adapted from Pearson and Faux [52].

Here, f is the degree of truncation of the pyramid (see Fig. 10). With the volume of integration given by Eq. (29), and using the method developed in Ref. [60] (described in the preceding pages), Pearson and Faux [52] arrived at complex but, nevertheless, closed-form solutions for the stress distribution of pyramidal shaped and illustrated their results for the InAs-GaAs system (relying on the experimental data from Fry et. al. [53] for the geometry in Fig. 10). They also investigated QDs with nonuniform composition. In such a case, the pyramidal QD is sliced into a large number of smaller truncated pyramids, and the small slices are assumed to have uniform composition. Several aspects of their results are of interest. As the reader will gather from Fig. 11 (specific to InAs-GaAs), the magnitudes of the strain components were found to be the largest at the QD/matrix interface (at $x_3 = 55$ nm), especially at the vertices with the strain attenuating rapidly in the barrier material. This is consistent with the notion that classical continuum elasticity admits a singular solution close to the vertices. Also, the strain distribution in the matrix material immediately below the square face remains unchanged for different truncations (f) considered because the base of the pyramidal dot remains unchanged. ε_{11} and ε_{22} are compressive through out the dot though lesser in magnitude than the initial misfit strain of -6.7% owing to strain relaxation. Outside the dot, ε_{33} is compressive within the barrier material owing to the QD relaxing outward along x_3 , compressing the local host material in the process. Interestingly, as a

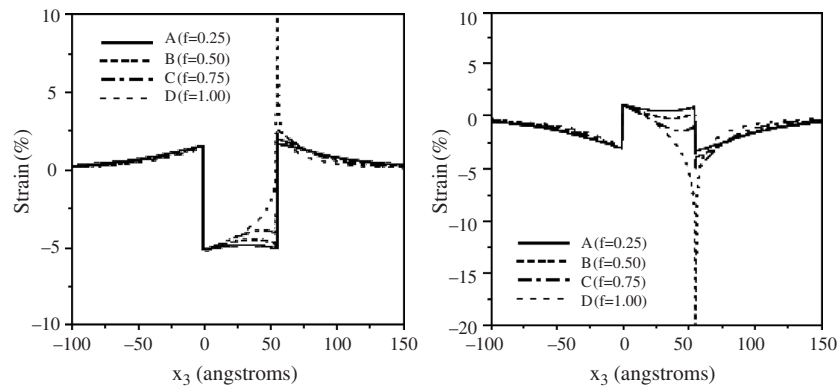


Figure 11. Illustration of the variation of ε_{11} (left) and ε_{33} (right) traced along x_3 obtained by analytical calculations on a pyramidal quantum dot (based on actual InAs/GaAs quantum dot geometry because of Fry et al. [53]) by Pearson and Faux [52]. The height of the dot is 55 \AA . (The base of the dot is located at $x_3 = 0$ and the apex at $x_3 = 55$ angstroms). Lines A, B, C, and D represent the different truncation factors “ f ” considered in the above analysis. Reproduced with permission from [52], Pearson et al., *J. Appl. Phys.* 88, 730 (2000), Figs. 2, 6. © 2005, American Institute of Physics.

result of this, ε_{33} tends to overrelax inside the dot with tensile strains existing in QDs with low truncation factors (compare with Fig. 11). However, Pearson et al. [52] note, as the truncation factor is made higher, the Poisson effect of ε_{11} and ε_{22} is much reduced which results in a compressive ε_{33} in the QD.

In the analysis of Pearson and Faux [52], dots with graded composition exhibited smaller strains at the base because the mismatch strain is lower at the base for this case (compared against dots with uniform composition of InAs). The other trends follow patterns similar to the instance of QDs with uniform InAs composition discussed hitherto. In yet another case of an array of QDs discussed in Pearson et al. [52], superposition of tensile stresses of adjacent material results in further relaxation of the compressive strain component ε_{11} of the QD in the center of the array. ε_{33} is always compressive within the dot in an array (compare this with the isolated quantum dot) due to the compressive stresses of the surrounding material superposing with the small tensile stress.

Davies [54] drew an analogy with the Poisson equation of electrostatics and the lattice mismatch induced strain problem in quantum dots. In a treatment that can be easily related to that of Eshelby [30] as well as Downes et al. [49], he formulated solutions of spherical, cuboidal and pyramidal dots. In this analogy, lattice mismatch plays the role of charge density. Alternatively, as discussed by Eshelby [30], the mismatch transformation strain may be considered the density of an astronomical body while the dilation is related to the Laplacian of the “gravitational” potential of the quantum dot or inclusion shape.

Several works [55–61] have resolved strain distribution in different shapes via numerical methods. For example, Shin et al. [61] used the finite element method and analyzed structures similar to those in Faux and Pearson’s work [52]. Additionally, Shin et al. [61] also reported the change in strain distribution with change in dot truncation as a function of stacking period. Some representative pictures and results from Shin et al. [61] are shown in Figs. 12 and 13.

2.2.3. Atomistic versus Continuum Calculations of Strain Distributions in QD/QWRs

A few of the works have resorted to atomistic calculations for strain distributions [61–64]. Since by the very nature and size scale of the lattice mismatch embedded quantum dot problem, millions of atoms have to be considered, *ab initio* methods are computationally too intensive. Empirical force-field molecular dynamics must be resorted to. The accuracy and the value of empirical force field atomistic calculations lie in the choice of a suitable potential. The latter is either fit to available experimental data for the material under consideration or alternatively may be developed using *ab initio* methods. As pointed out by Pryor et al. [58], atomistic methods are faithful to the true point symmetry of the material while analogous continuum models may not necessarily reflect this in their coarse-grained sense. Further nonlinearities (anharmonic effects) are automatically embedded in an atomistic formulation. (However, to be accurate, the potential must have been parameterized appropriately to account for anharmonic effects.)

The valence force field (VFF) [65] provided by Keating [66] and Martin [67] is perhaps the simplest. Anharmonicity is inadequately accounted for in this approach and only nearest neighbors are accounted for. Stillinger-Weber [68–71] potentials and Tersoff potentials are more involved. Stillinger-Weber potentials have been applied to Si/Ge QDs [69–71]. The Tersoff potential has been used for InGaAs/GaAs quantum dots [72]. Kikuchi et al. [190] have compared the VFF and Stillinger-Weber potential for the SiGe/Si system and conclude that for smaller quantum dots, the Stillinger-Weber potential may be better as VFF yields some physical results in the strain profiles (see also Ref. [191]).

Notably, Pryor et al. [58] have presented an interesting comparison between continuum elasticity and atomistic simulations (Fig. 14). For large mismatch strains (e.g., 7% strain mismatch for InAs/GaAs quantum dots) only minor discrepancies from continuum elasticity were found (Fig. 14). Other groups have similarly found that continuum elasticity for most cases provides reasonable answers, for all practical purposes, even at the monolayer level [63, 73].

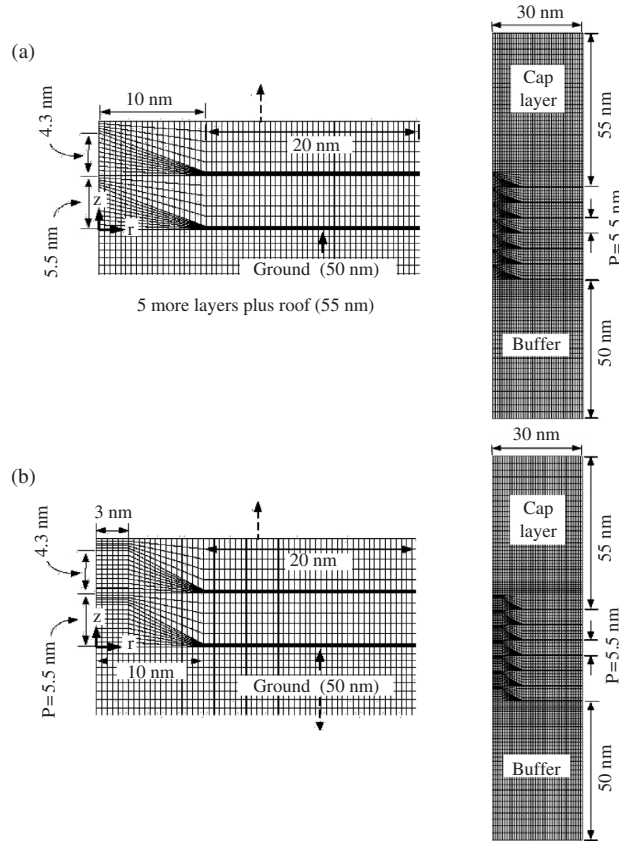


Figure 12. Shin et al.'s finite element model of the multilayer-stacked InAs/GaAs structure with (a) truncated (b) un-truncated quantum dots. Reproduced with permission from [61], Shin et al., *J. Phys.* 15, 3689 (2003), Fig. 1. © 2003, IOP Publishing Limited.

Tadić et al. [59] have also made a comparative study of strain distribution in cylindrical InAs/GaAs and InP/InGaP QDs as obtained from isotropic elasticity theory, anisotropic elasticity and atomistic simulations [42]. Davies' approach [54] outlined above was used for the isotropic case, while finite element method was employed for the anisotropic case. For the

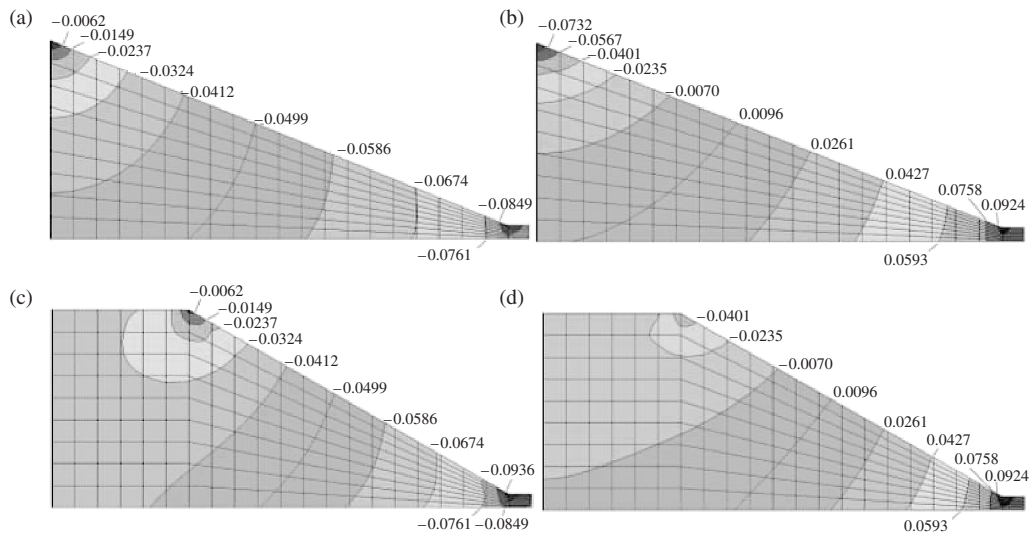


Figure 13. Comparison of the radial and axial strains along the midplane for (a) ϵ_{rr} contours for untruncated pyramidal quantum dot. (b) ϵ_{zz} contours for untruncated pyramidal quantum dots. (c) ϵ_{rr} contours for truncated quantum dots. (d) ϵ_{zz} contours for truncated quantum dots in the midlayers (of the array) with a stacking period of 7 nm. Reproduced with permission from [61], Shin et al., *J. Phys.* 15, 3689 (2003), Fig. 1. © 2003, IOP Publishing Limited.

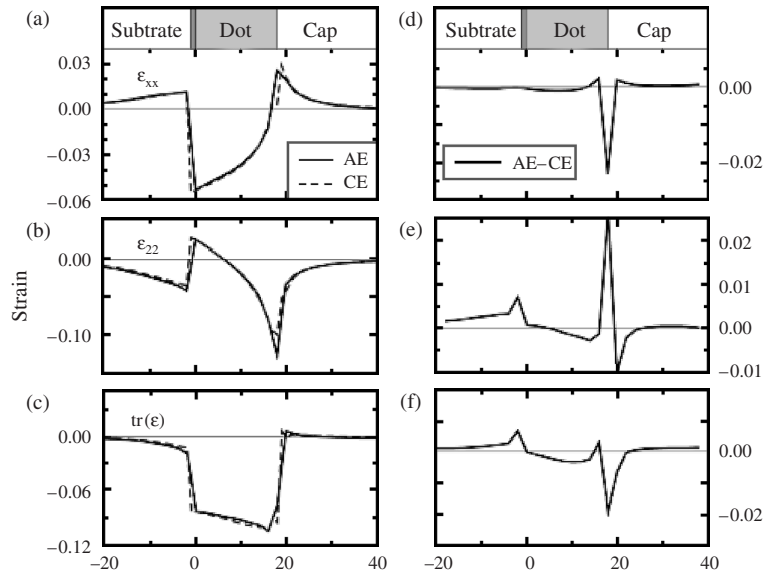


Figure 14. Strain components along the axis of a square InAs pyramidal quantum dot with [110] faces buried in GaAs host. Solid lines are obtained by valence force field (depicted as AE) and dashed lines are from continuum elasticity methods. (a)–(c) Strain distributions; (d)–(f) the difference between these two approaches. The scale for a–c differs from that for d–e. Reproduced with permission from [67], Pryor et al., *J. Appl. Phys.* 83, 2548 (1998), Fig. 5. © 1998, American Institute of Physics.

atomistic simulations, both VFF and Stillinger-Weber potentials were used and compared. Better agreement was found between the strain contours between the four methods employed for InP/InGaP QDs than in InAs/GaAs QDs. This observation was attributed to the smaller lattice mismatch in the InP/InGaP system. In particular, differences are only observed in regions where strain changes very rapidly, that is, the edges and corners of the structures.

2.2.4. Quantum Wires

Some of the early literature on shape dependence effects on quantum dots strain focused on quantum wires (QWR), which are one-dimensional analogues of quantum dots (zero dimensional). In particular, much emphasis was placed on solving problems for specific QWR or QD shape. A strained QWR (Fig. 15) is a region of material that has two of its dimensions very small in comparison to the third. The cross-sectional size of the wire is of the order of a few tens of nanometers giving rise to quantum confinement of electrons in these two spatial dimensions. Eshelby's formalism [30] can be readily employed to tackle various shaped QWRs. A QWR with a uniform circular cross section (see Fig. 15) surrounded by an infinite host matrix happens to be a special case of an ellipsoidal inclusion in an infinite medium and Eshelby's well-known solution [30] for such ellipsoidal inclusions, discussed earlier, can be invoked to find the strain and displacement fields.

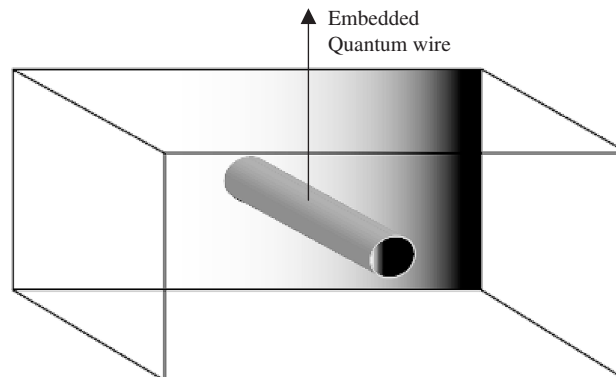


Figure 15. A quantum wire in the form of an infinite elliptical cylinder embedded in an infinite medium.

Notwithstanding early analytical work on thin films or islands present in the vicinity of a free surface [38–44], Downes and Faux [74] were among the first to explicitly deal with the problem of analytical strain-distribution calculation for buried strained layers; the case of a quantum wire with square cross section degenerating to a special instance of this more general problem. The problem addressed by Downes and Faux [74] is schematically depicted in Fig. 16, which illustrates a buried strained layer (Ω) surrounded by an infinite host matrix (D). The dimension of the structure in the z -direction is assumed to be very large so that plane strain conditions apply.

Downes and Faux [74] proposed an approach similar to one already outlined for the three dimensional case (Downes et al. [49]). (However, we note that, chronologically, the two-dimensional work preceded the three-dimensional formulation even though we have discussed the latter in an earlier section.) They obtained (for the problem in Fig. 16)

$$\sigma^{\text{layer}}(x, y) = \int_{-l}^{+l} \int_{-c}^{+c} \sigma^{\text{cyl}}(x - x_0, y - y_0) dy_0 dx_0 \quad (31)$$

The stress fields for “point” cylindrical inclusion serve as Green’s function for this problem. They are

$$\sigma_{xx}^{\text{cyl}} = \Upsilon(x^2 - y^2) \quad (32a)$$

$$\sigma_{yy}^{\text{cyl}} = \Upsilon(y^2 - x^2) \quad (32b)$$

$$\sigma_{xy}^{\text{cyl}} = \Upsilon(xy) \quad (32c)$$

$$\Upsilon = \frac{\Lambda_2}{(x^2 + y^2)^2}; \quad \Lambda_2 = \frac{E \varepsilon^m}{2\pi(1 - \nu)}$$

Explicit analytical expressions (Eqs. [33]) have been provided by Downes and Faux [74] for a single strained layer after evaluating the integral in Eq. 31

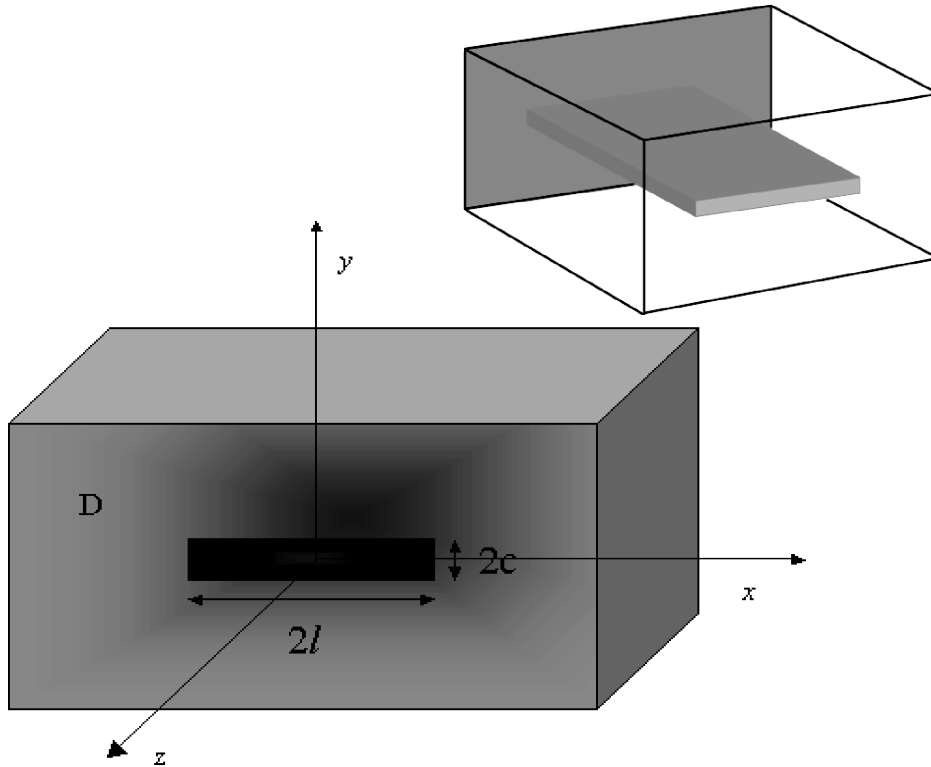


Figure 16. Illustration of a cross section through a buried strained layer. (Inset three-dimensional rendering of a strained layer). Adapted from Downes and Faux [74].

$$\sigma_{xx} = \Lambda_2 \left[\sum \tan^{-1} \left(\frac{l \pm x}{c \pm y} \right) \right] \quad (33a)$$

$$\sigma_{yy} = \Lambda_2 \left[\sum \tan^{-1} \left(\frac{c \pm y}{l \pm x} \right) \right] \quad (33b)$$

$$\sigma_{xy} = \frac{\Lambda_2}{2} \left[\sum p \ln \{ (l \pm x)^2 + (c \pm y)^2 \} \right] \quad (33c)$$

Once again, the summation is over various combinations of + and -. In Eq. (33c), p is +1 for odd number of plus signs and -1 for even number of plus signs.

The strained layer reduces to a quantum wire with square cross-section when l equals c (Fig. 16). From the expressions for the strain field in and around a quantum wire with a square cross section, one can deduce that only a small fraction of the lattice mismatch strain is accommodated across the cross-section of the wire, with considerable strain relaxation occurring along these shorter dimensions [75].

Quantum wires are often synthesized *in situ* as arrays and also occur in device structures (say, e.g., lasers, see Fig. 17) as periodic arrangements [76–79].

Considering a periodic array of trapezium-shaped wires buried in an infinite medium (Fig. 18), Gosling and Willis [80] tackled the array problem by simulating each of the wires to be an Eshelby-like inclusion. Modeling trapezium-shaped QWRs as inhomogenities (with elastic constants different than the surrounding host material) can considerably complicate calculations; consequently, same elastic constants are chosen for the quantum wires and the matrix. Further assuming all materials to be isotropic, and employing the elastic Green function and Fourier transformations, exact analytical expressions for the stress field were provided [80].

As can be inferred from Fig. 18, the case of a buried strained epitaxial layer can be recovered when one allows “ w ” to equal “ p .” Also by allowing $p \rightarrow \infty$, the case of an isolated wire can be examined. Gosling and Willis [80] applied these expressions to compare the structural stability and electronic properties of an array of wires with that of an isolated wire and found that for array periods of five wire widths or more the stability (see Ref. [81–87] for literature on stability issues in nanostructures) and band-gap characteristics of the periodic arrangement were similar to those of isolated wires.

Faux et al. [88] have employed the stress field because of a point cylindrical inclusion (similar to the way the point sphere stress solution was applied in the three-dimensional case [49]) as a “Green function” to calculate the stress field about an arbitrarily shaped QWR buried in an infinite medium. Analogous to the reduction of the three-dimensional volume integral to a surface integral in the case of arbitrary-shaped quantum dots [49], their scheme reduces the problem to the evaluation of a path integral around the boundary of

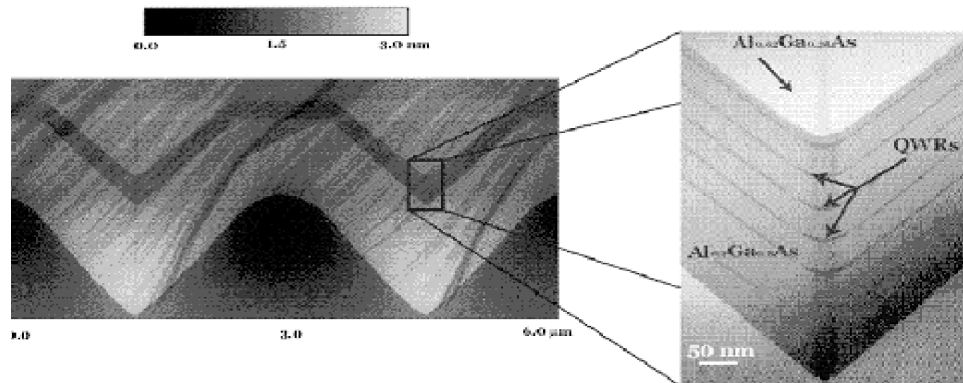


Figure 17. AFM cross-section image (left) of two V-groove QWR lasers separated by a distance of $3 \mu\text{m}$. TEM cross-section image (right) of a single V-groove QWR laser with five vertically stacked QWRs in the waveguide core. Reproduced with permission from [79], Weman and Kapon, www.ifm.liu.se/matephys/nanopto/QWRs.html, © 2005, Weman.

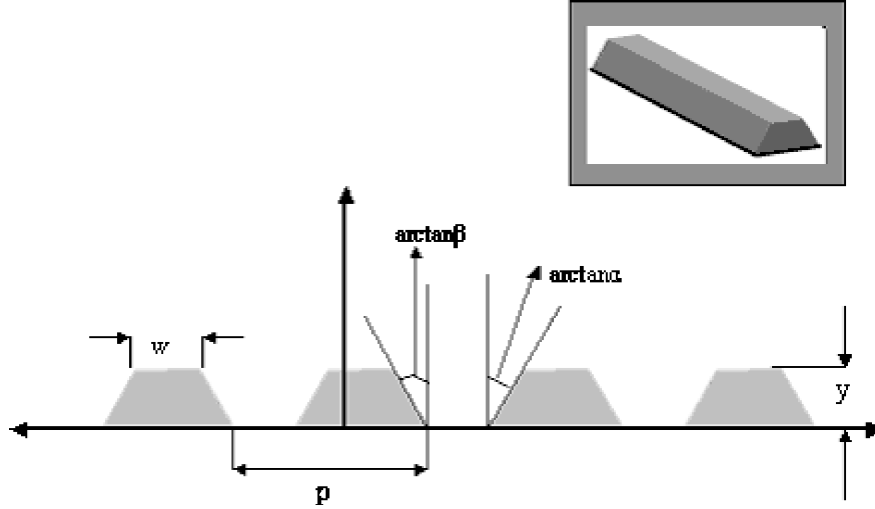


Figure 18. Schematic of a periodic array of trapezoidal quantum wires illustrating the geometry of the wire. “ p ” is the period of the array, “ w ” is the width of each wire at the apex, “ y ” is the height of the wire. The characteristic angles are also shown. (Inset: a three-dimensional rendering of the trapezoidal quantum wire). Adapted from Gosling and Willis [80].

the quantum wire. Consider the three vectors [88]:

$$\begin{aligned} \mathbf{A}_{xx} &= -D_2 y \mathbf{i}; & \mathbf{A}_{yy} &= D_2 x \mathbf{j}; & \mathbf{A}_{xy} &= \frac{D_2}{2} (x \mathbf{i} - y \mathbf{j}) \\ D_2 &= \frac{\Lambda_2}{x^2 + y^2}; & \Lambda_2 &= \frac{E \varepsilon^m}{2\pi(1 - \nu)} \end{aligned} \quad (34)$$

Similar to the three-dimensional case [49], the vectors of Eq. (34) are chosen such that $\nabla \times \mathbf{A}$ yields the cylindrical Green’s function components σ_{xx} , σ_{yy} , and σ_{xy} which are given by Eq. (32).

With the aid of Eqs. (32) and (34), the stress distribution due to a quantum wire with arbitrary cross section was obtained by evaluating the following surface integral [88]:

$$\boldsymbol{\sigma}(\mathbf{r}) = \int \nabla \times \mathbf{A}(\mathbf{r} - \mathbf{r}') \cdot d\mathbf{S}(\mathbf{r}') \quad (35)$$

The integration is performed over the area of the QWR. With the application of Stokes theorem, this surface integral (Eq. [35]) was reduced to a line integral around the boundary of the wire [88]:

$$\boldsymbol{\sigma}(\mathbf{r}) = \oint \mathbf{A}(\mathbf{r} - \mathbf{r}') \cdot d\mathbf{r}' \quad (36)$$

For simple geometries such as rectangular wires, the line integral in Eq. (36), can be performed analytically providing, for example, similar results to the strained layer case visited earlier. For QWRs with a rectangular cross section, Faux et al. [88] have noted that with a proper choice of the integrand, only the horizontal boundaries of the rectangular QWR can be made to contribute to σ_{xx} and only the vertical boundaries to σ_{yy} , which simplifies the computation further. Faux et al. [88] apply their methodology to an InP wire of triangular cross section embedded in GaAs host with a lattice mismatch strain, $\varepsilon^m = -3.7\%$. Nishi et al. [89] have also performed strain calculations on the exact same wire configuration using the finite element method. For the triangular cross section, some results are illustrated in Fig. 19 [88]. They are found to agree well with Nishi et al.’s [89] results.

As Faux et al. [88] have noted from Fig. 19, significant strain relaxation is found to occur over most of the area of the wire with the magnitude of the strain components ε_{xx} and ε_{yy} being less than about $\varepsilon^m/2$ at all points in the QWR, except at the apex of the triangle. Further, ε_{xx} is least relaxed at the base resulting in over-relaxation of ε_{xx} , which is manifest

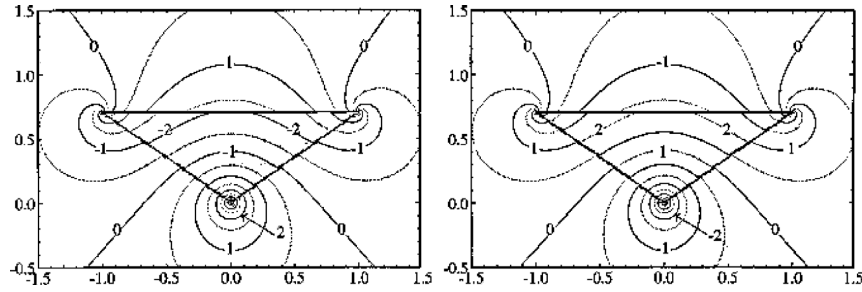


Figure 19. Strain contours (in % units) ε_{xx} (left) and ε_{yy} (right) for an InP triangular wire within an infinite GaAs matrix. The initial misfit strain is assumed to be 3.7%. Reproduced with permission from [88], Faux et al., *J. Appl. Phys.* 80, 2515 (1996), Fig. 1. © 1996, American Institute of Physics.

in the positive values that ε_{yy} assumes. In agreement with inclusion theory, the trace of the strain tensor is constant for all points in the inclusion.

For complicated shapes the QWR boundary may be discretized and the contour integral can be converted into a summation. Arbitrary shapes can be approximated to be composed of a combination of line elements and circular arcs. In some cases, this decomposition may be exact. By employing the simple expressions for line elements, and so forth, contributions due to a line element and a circular arc, stress/strain evaluations can be obtained. In fact, precisely on these lines, Downes et al. [90] in a subsequent work have provided analytic expressions for the strain field due to a lattice-mismatched QWR whose cross section is composed of any combination of line elements and circular arcs. The authors applied this methodology to GaAs/AlGaAs crescent-shaped wire [90]. Typically, crescent-shaped quantum wires are grown *in situ* using organometallic chemical vapor deposition of thin layers on V-grooved substrates. The position of the QWR is germinated at the position of the initial groove on the patterned substrate, leading to highly self-ordered wire arrays.

As illustrated in Fig. 20, the wire was approximated as consisting of two lines and two arcs [90] (the thin quantum wells on the valley sides (not shown in Fig. 20) are usually ignored). For a given radius of curvature of the lower arc and a given thickness of the QWR (this data obtained from Kapon et al. [76] for the GaAs/AlGaAs system), the radius of curvature of the upper arc can be arrived at (using geometry) and the strain contours inside and outside the QWR were obtained (Fig. 21).

Decomposition of the crescent shape into line and arc elements

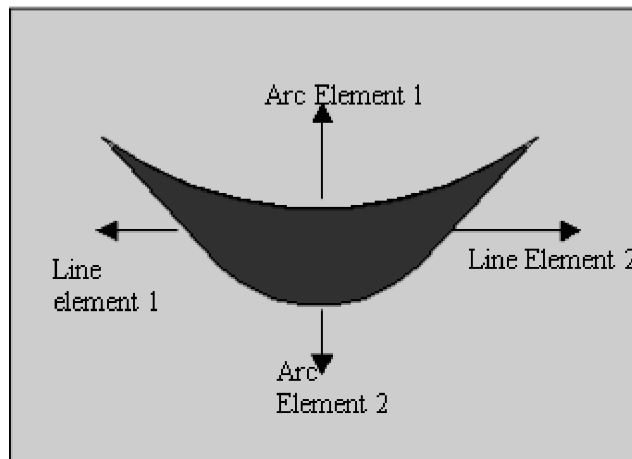


Figure 20. Decomposition of the boundary of a crescent shaped wire into line and arc elements. Adapted from Downes et al. [90].

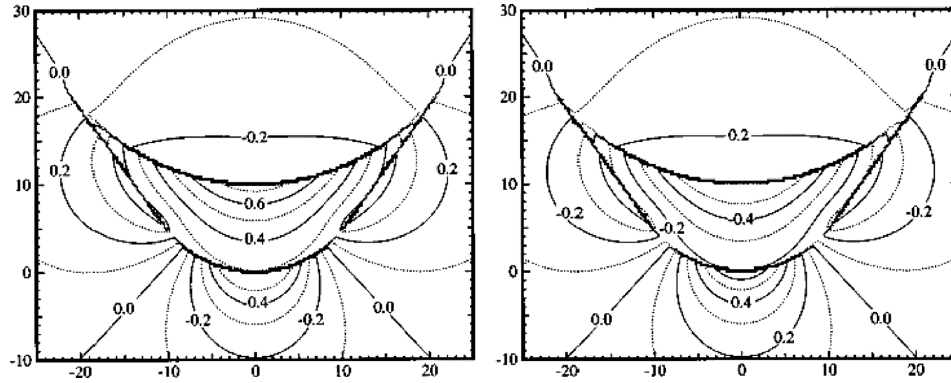


Figure 21. Strain contours in units of percent indicating ϵ_{xx} (left) and ϵ_{yy} (right) for a GaAs/AlGaAs crescent-shaped wire (geometry of wire based on Kapon et al. [76]) with initial misfit strain of 1%. Reproduced with permission from [90], Faux et al., *J. Appl. Phys.* 82, 3754 (1997), Fig. 6. © 1997, American Institute of Physics.

As can be observed in Fig. 21, Downes et al. [90] noted that, for an initial misfit strain of 1% (the wire is initially under tensile strain), the maximum strain in the x -direction is about 0.75% (at the center and near the top of the wire, where the width is the largest). ϵ_{yy} is negative within the QWR. Expectedly, the dilation is constant inside the wire (zero outside the wire). In a rectangular QWR with a high-aspect ratio, the strain relaxation occurs predominantly in one dimension (ϵ_{yy} would be about -0.9% and ϵ_{xx} would tend to ϵ_0). The crescent-shaped QWR has smaller peak strain values because strain relaxation occurs in two dimensions.

Provided wires of the same thickness are considered, on incorporation of the thin lateral quantum wells, the strain fields have been observed to be similar [90] except at the corners of the structure. This similarity finds reason in the fact that as the QWs are thin, the contour integral contribution along the lower line of the well is almost cancelled by the contribution because of the upper line.

We have seen that almost all the analyses discussed far assume identical elastic constants for the quantum dot and the barrier material, which begets the question whether this kind of treatment is justified. Clearly, for the ellipsoidal shape quantum dots embedded in an unbounded matrix, Eshelby's equivalent inclusion method [30] provides an easy recipe to account for modulus mismatch. More generally, this is not easy. So are we justified in using the same elastic constants for both the materials? Downes and coworkers [90] have outlined the following issues to consider: (1) Two different materials, at least, are used. (2) The materials are generally semiconductor alloys. (3) At least one of the materials is in a state of strain (It is difficult to estimate the elastic constants for alloys in a state of strain.) Downes and co-workers [90] argue that Keyes scaling relationship [91–92] for III–IV semiconductors suggests that it is appropriate to choose the elastic constants of the barrier material for all materials in the system because all materials have the same lattice spacing before misfit strain relaxation takes place. As an illustration, the elastic constants for a strained InAs QD in a GaAs matrix will be closer to the GaAs values than those for unstrained InAs. In the present authors opinion, this issue requires further investigation. If necessary, the modulus mismatch can be accounted for as a perturbation (see, for example, Andreev et al. [93]).

2.3. Effect of Presence of a Free Surface in Near Vicinity

Because of their mode of fabrication and operation, QDs/QWRs are most often buried fairly close to a free surface rather than being embedded in an “infinite” matrix where the most material boundaries play no role. Such “shallowly” buried quantum dots act like stressors and the resulting elastic fields coerce vertical dot ordering during growth of subsequent layers of self-assembled quantum dots. (Lateral ordering of dot layers is known to occur in the presence of regular dislocation arrays or buried strained layers [94–95].) Furthermore, both qualitatively and quantitatively, the strain behavior of embedded QD/QWRs that are located close to a free surface is quite different from one embedded in an infinite medium. For example, the famous Eshelby rule that an ellipsoidal shaped inclusion with a uniform

misfit will admit a uniform elastic state no longer holds true. For some simple shapes and cases, closed-form results are available although given the complications in satisfying the traction free boundary conditions at the host material boundaries, resort must be made toward numerical methods. As already indicated, typically, if the distance of a quantum dot from the free surface is larger than $3R$ (in case of a spherical dot), an infinite space solution may be invoked with reasonable accuracy. Otherwise, the so-called half-space solution is recommended. The schematic of the semi-infinite domain (defined by $x_3 \geq 0$) is shown in Fig. 22 below:

In the context of half-space, Mindlin and Cheng's seminal work [96–97] addressed a center of dilatation. This solution can be elegantly expressed in terms of the thermoelastic potentials of an infinite solid [98]. Following Mindlin and Cheng [96–97], we briefly discuss the displacement field of a spherical dot buried at depth, h , from the free surface. Isotropicity is assumed and both the QD and the matrix are assumed to have identical elastic moduli.

The relation for displacement $\mathbf{u}(\mathbf{r})$ in a semi-infinite region $0 \leq z$ with a free surface at $z = 0$ as provided by Mindlin and Cheng is [97]:

$$4\pi\mathbf{u}(\mathbf{r}) = -\nabla\phi - \nabla_2\phi_2 \quad (37)$$

where ϕ is the harmonic potential of the infinite system given by Eq. (24) and ϕ_2 is the reflection transform of ϕ in the plane $z = 0$. For an *infinite* solid Goodier [98–99] showed that (for purely dilatation axisymmetric problems) the displacement potential obeys the following Poisson's equation:

$$\nabla^2\phi = -4\pi\frac{1+\nu}{1-\nu}\varepsilon^m = -4\pi\frac{9K}{3K+4\mu}\varepsilon^m \quad (38)$$

The operator ∇_2 is given by [97]

$$\nabla_2 = (3 - 4\nu)\nabla + 2\nabla z \frac{\partial}{\partial z} - 4(1 - \nu)\hat{e}_z \nabla^2 z \quad (39)$$

The radii to a point of interest (x, y, z) from $(0, 0, h)$ and its image point $(0, 0, -h)$ are, $r = [x^2 + y^2 + (z - h)^2]^{1/2}$ and $r_2 = [x^2 + y^2 + (z + h)^2]^{1/2}$, respectively. Thus ϕ and ϕ_2 are [97]

$$\begin{aligned} \phi &= \frac{4\pi a^3 \varepsilon^m}{3R}, & \phi_2 &= \frac{4\pi a^3 \varepsilon^m}{3R_2} & \text{for } r \geq a \text{ (exterior to the dot)} \\ \phi &= \frac{2\pi \varepsilon^m (3a^2 - R^2)}{3}, & \phi_2 &= \frac{4\pi a^3 \varepsilon^m}{3R_2} & \text{for } r < a \text{ (points inside the dot)} \end{aligned} \quad (40)$$

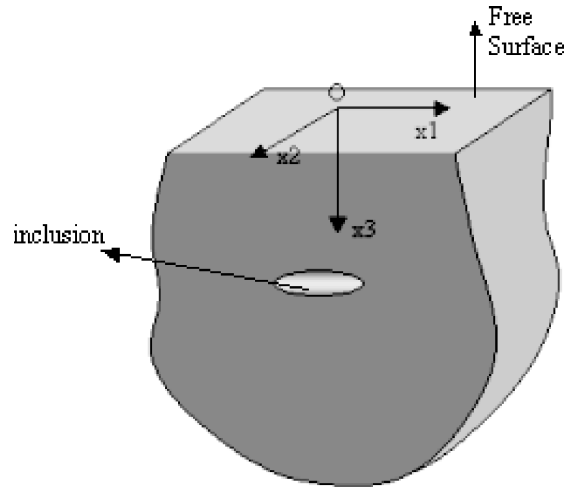


Figure 22. Illustration of a semi-infinite space with a plane free surface ($z < 0$). An embedded inclusion can also be seen.

From Eq. (26), we have the solutions for displacements as [97]

$$\begin{aligned} \mathbf{u}_e &= \frac{a^3 \varepsilon^m}{3} \left[\frac{\mathbf{r}}{r^3} + \frac{(3-4\nu)\mathbf{r}_2}{r_2^3} - \frac{6z(z+h)\mathbf{r}_2}{r_2^5} - \frac{2\mathbf{k}}{r_2^3} \{(3-4\nu)(z+c) - z\} \right] \quad \text{for } r > a \\ \mathbf{u}_i &= \mathbf{u}_e + \frac{a^3 \varepsilon^m \mathbf{r}}{3} \left(\frac{1}{a^3} - \frac{1}{r^3} \right) \quad \text{for } r < a \end{aligned} \quad (41)$$

Where \mathbf{u}_e is the displacement field for an exterior point, and \mathbf{u}_i is the displacement field for a point inside the quantum dot. The strain field can be recovered in the usual manner from strain-displacement relationships.

Davies [100] has extended Mindlin and Cheng's [97] approach. He showed that the displacements and strains for the semi-infinite solid can be, in a rather simple manner, expressed in terms of those for an infinite solid and their corresponding derivatives normal to the surface. He finds the following expression for displacement [100]:

$$u = u^\infty + (3-4\nu)\bar{u}^\infty + 2z \frac{\partial}{\partial z} (\bar{u}_x^\infty, \bar{u}_y^\infty, -\bar{u}_z^\infty) \quad (42)$$

where

$$\bar{u}^\infty(x, y, z) = u^\infty(x, y, -z) \quad (43)$$

The displacement at the free surface, which can be obtained by setting $z = 0$, is found to be increased by a factor of $4(1-\nu)$ compared to the displacement of the same plane in an infinite solid. The same factor relates the strains at the free surface: ε_{xx} , ε_{yy} , and ε_{xy} to their counterparts in the infinite sample. As noted by Davies [100], part of this enhancement occurs because the QD/QWR is less contained by a free surface than in an infinite solid but the remaining part is due to less obvious effects arising out of distortion of the surrounding which pushes the inclusion toward the surface. A dilation of $-4(1-2\nu)\bar{\varepsilon}_{zz}^\infty$ arises due to the presence of the free surface. Unlike the infinite medium case, the dilation is neither uniform within the QD/QWR nor zero outside it.

Alternative (although essentially equivalent) methods are also available to solve such semi-infinite problem for shallowly embedded QD/QWRs. Many problems of elasticity can be simplified by reducing to force distribution problems over some region, which then can be solved through use of Green function techniques. The Green function for the half-space (Eq. [44]) (corresponding to Fig. 22) was derived by Mindlin [101]:

$$G_{ij}(\mathbf{x}, \mathbf{x}') = \frac{1}{16\pi\mu(1-\nu)} \left[\begin{aligned} &\frac{3-4\nu}{r} \delta_{ij} + \frac{1}{r^2} \delta_{ij} + \frac{(x_i-x'_i)(x_j-x'_j)}{r^3} + \\ &\frac{(3-4\nu)(x_i-x'_i)(x_j-x'_j)}{r_2^3} + \frac{2x_3x'_3}{r_2^3} \left\{ \delta_{ij} - \frac{3(x_i-x'_i)(x_j-x'_j)}{r_2^2} \right\} + \\ &\frac{4(1-\nu)(1-2\nu)}{r_2+x_3+x'_3} \left\{ \delta_{ij} - \frac{(x_i-x'_i)(x_j-x'_j)}{r_2(r_2+x_3+x'_3)} \right\} \end{aligned} \right] \quad (44)$$

In Eq. (44), the effect of the free surface occurs through the terms containing r_2 . Subsequently, Seo and Mura [102] and Chiu [50] employed the half-space Green's function to obtain the Eshelby tensor for dilating ellipsoidal and cuboidal inclusions respectively (in a manner similar to Eq. [14]). For the case of an ellipsoid, closed form expressions are possible only when two of the semi-axes of the ellipsoid are equal [35].

On the lines of the preceding discussion, an interesting work is due to Glas [44]. Consider a uniformly thick layer of a semiconducting material coherently deposited on a substrate and covered by a capping layer of the same substrate material (Fig. 23). Such embedded layers frequently develop nonuniform mismatch strains either due to spatial distribution of temperature or variations in the composition of the quantum well material.

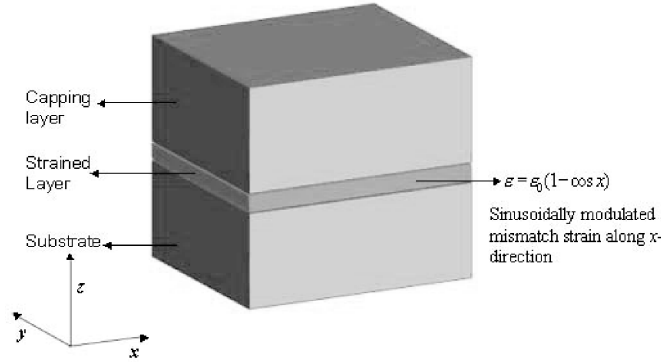


Figure 23. Illustration of a buried strained layer, with a sinusoidally modulated dilational mismatch strain, in the presence of a free surface as considered by Glas et al. [36].

Glas [44] using an Eshelby-like cutting and welding *gendaken* combined with the method of images (to account for the boundary conditions) obtained an analytical solution to a sinusoidally modulated dilatational mismatch strain problem. The relaxation of a general misfit dilational inhomogeneity was obtained in the form of an integral, which can be evaluated when the stress-free strain admits a simple Fourier transform. Glas [44] applied his method to a coherent parallelepipedic inclusion (rectangular quantum wire) and to a step formed at the interface between a substrate and a coherent capping layer to arrive at fully analytical solutions.

Further, in a later work, Glas [103] also provided a closed-form solution for the strain fields of truncated fourfold pyramidal QDs and trapezoidal QWRs buried in half-space. To solve the problem, the pyramidal QDs were decomposed into elementary cuboids of infinitesimal height and varying areas. The displacements obtained from each of them were then summed up to obtain the net displacements by superposition principle. Glas [104] extended his solution of a single QD to the study of buried QD arrays and later periodic arrays of QWRs in half-space [105]. Starting with the cases of single and periodic trapezoidal wires in half space, the calculation is extended to QWRs of arbitrary polygonal section. Analytical formulae for strain fields have also been found for a right-angled triangular section lying in half-space using results for those of a semi-infinite rectangular slab and a semi-infinite beveled slab.

Barabash and Krivoglaz [106] employed Fourier transform of the displacement field due to a random distribution of point inclusions submerged under a plane with a given density-depth profile. The relaxation of the displacement was determined as a one-dimensional Laplace transform of the inclusion density.

Romanov et al. [107] compared the dilation of strain obtained for cuboidal and trapezoidal QDs using finite element method with analytical expressions provided for an spheroidal inclusion (with the same volume as the trapezoidal and cuboidal inclusion) [92] buried at identical depths. Except at the interface between the dot and the matrix (i.e., in the immediate vicinity of the dot), the spheroidal inclusion model provided good approximation to the finite element models of the cuboidal and trapezoidal inclusions (for both isolated and periodic inclusion models) even at significantly shallow levels of submergence, following which Romanov et al. [107] have suggested using the ellipsoidal inclusion model to obtain reasonable (if not very accurate) estimates of stresses for most geometries of dots.

2.4. Effect of Material Anisotropy and Nonlinearity

2.4.1. Anisotropic Effects

Most semiconductor compounds crystallize to cubic crystallinity. Against the isotropic value of 1, the anisotropy coefficient (defined as $C_{11}-C_{12}/2C_{44}$) for most III–IV semiconductors is around 0.5. For some cases, the assumption of elastic isotropy may be justified or alternatively the uncertainty in other material and configurational parameters (e.g., lattice parameters, dimensions, etc.) may far exceed the error due to neglect of the anisotropic effects. In

fact, some authors suggest that the isotropic approximation is reasonable for some cases of the two-dimensional problems [108]. (Caution should be exercised in taking this statement too literally and broadly. The reader is referred to Ref. [108] for further details.)

Explicit analytical expressions for the anisotropic Green's functions are unavailable (except for hexagonal symmetry) so the oft-used technique of reducing an elastic problem to a force-distribution problem cannot be employed readily. For the cubic anisotropic case, approximate solutions for the point force equation can be realized perturbatively and thus are applicable only for weakly anisotropic materials. Dederichs and Liebfried [109] have investigated different approaches for the estimation of approximate cubic Green's function [see also Ref. 110–112].

Starting with the point-force formalism of Green's functions and assuming identical elastic constants for both the QD and the host material, Andreev et al. [93] suggested a general analytical method for the Fourier transform of the anisotropic Green function and presented explicit results for cubic crystals (in Fourier space). With this analytical result in hand, the expression of the Fourier transform of the strain tensor was also obtained. In their results, the shape effect of the quantum dot structure appears as the Fourier transform of a characteristic shape function. Equation (45) provides the Fourier-space strain solution [93]:

$$\tilde{\epsilon}_{ij}^s(\xi) = \varepsilon^m \tilde{\chi}_{QD}(\xi) \left\{ \begin{array}{l} \delta_{ij} - \frac{(C_{11} + 2C_{12})\xi_i\xi_j/\xi^2}{1 + (C_{12} + C_{44})\sum \xi_p^2/C_{44}\xi^2 + C_{an}\xi_p^2} \\ \times \frac{1}{2} \left[\frac{1}{C_{44} + C_{an}\xi_i^2/\xi^2} + \frac{1}{C_{44} + C_{an}\xi_j^2/\xi^2} \right] \end{array} \right\} \quad (45)$$

$\tilde{\chi}_{QD}(\xi)$ is the transformed characteristic shape function of the quantum dot structure defined by

$$\begin{aligned} \chi_{QD}(\mathbf{r}) &= 1, & r \text{ being a point inside the inclusion} \\ &= 0, & r \text{ being a point outside the inclusion} \end{aligned} \quad (46)$$

and C_{an} is given by

$$C_{an} = C_{11} - C_{12} - 2C_{44} \quad (47)$$

In the isotropic limit, $C_{an} = 0$ and the expression for the transformed isotropic strain simplifies to [93]:

$$\tilde{\epsilon}_{ij}^{iso}(\xi) = \varepsilon_0 \tilde{\chi}_{QD}(\xi) \left(\delta_{ij} - \frac{3\lambda + 2\mu}{\lambda + 2\mu} \frac{\xi_i\xi_j}{\xi^2} \right) \quad (48)$$

Transforming this strain back into real space and taking the trace, we recover the isotropic result discussed earlier (Andreev et al. [93] calculate the subtracted strain; that is, the mismatch strain is subtracted from the actual elastic strain. We have modified their expression to show the latter.):

$$Tr(\epsilon) = \varepsilon^m \frac{9K}{3K + 2\mu} \chi_{QD}(\mathbf{r}) \quad (49)$$

Equation (49) emphasizes the constancy of dilation within the QD and that it vanishes for points outside it. As evident from Eq. (45), this may not hold true for all shapes in the cubic anisotropic case.

Andreev et al. [93] also provide a comparison between isotropic and anisotropic models for cubic crystals. As mentioned earlier the degree of anisotropy can be characterized by the anisotropic coefficient, which is about 0.5 for III–IV semiconductors. As an example, the effective Poisson's ratio varies between 0.333 in the (001) direction to about 0.2 in the (111) direction. This variation in Poisson's ratio might be expected to result in a strong dependence of strain on the space direction. However, this was not found to be the case. In most cases where the "anisotropy" in shape of the QD is more than or equal to the anisotropy in the elastic properties, the dominant contribution to the strain distribution is caused by the

“anisotropy” in shape rather than the anisotropy in elastic properties. Figure 24 illustrates how the anisotropic solution of the radial component of the strain tensor ϵ_{rr} for a spherical InAs/GaAs quantum dot system (misfit strain of -3.7%) plotted along three directions, compares with the isotropic case.

As Andreev et al. [93] have pointed out, the influence of elastic anisotropy is small within the dot with both models yielding nearly the same constant value. Outside the sphere, however, anisotropy considerations are observed to produce significant deviations from the isotropic model. As a matter of fact, the isotropic model effectively gives the strain distribution averaged over the different directions outside the dot. For a cubic dot, with the symmetry of the elastic properties being the same as that of the geometry, the effect of elastic anisotropy is even smaller than for the spherical dot. Unlike the spherical quantum dot, the difference between the two models for a pyramidal QD, exhibiting lesser cubic symmetry than the elastic properties, was observed to be less outside the dot than inside it.

While an exact expression for Green’s function for the cubic case is not possible, it can be expressed in terms of a perturbation series where the first term is the isotropic Green’s tensor and the subsequent terms are correction terms of increasing order, converging to the full anisotropic result [113–114]. Faux and Pearson [115] exploited this notion and presented explicit (but approximate) Green’s tensors to permit rapid calculation of strain distribution in and around QDs. Computational effort is significantly reduced as excellent agreement was found with results of Andreev et al. [93] even with a first-order correction.

Pan and Yuan [116] expressed the half-space anisotropic Green’s function, for traction-free surface, as a sum of the infinite space Green function and an image part based on the extended Stroh formalism. The image part can be expressed as a one-dimensional integral. Using these Green functions, the elastic fields of a quantum dot can be expressed as simple integrals over the surface of the dot employing Betti’s reciprocal theorem. If the QD is a point source, then the strain fields can be expressed in analytical form. Other notable works on Green’s functions (assuming traction-free surface conditions) are due to Refs. [122, 126–128]. The reader may also refer to Pan [129], who in a later work, derived the anisotropic Green’s functions for generalized boundary conditions, based on the extended Stroh-formalism.

Pei et al. [122] investigated the elastic fields due to an array of lens-shaped anisotropic QDs buried under a capping layer of finite thickness using a three dimensional finite element method. The various geometrical parameters used in the model have been shown in

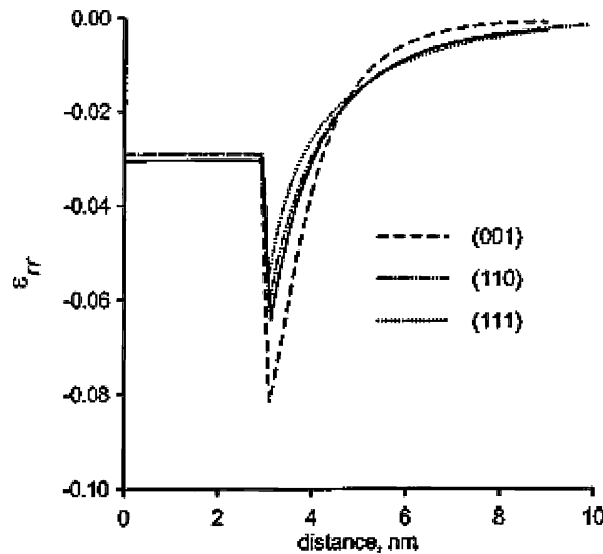


Figure 24. Radial strain tensor component ϵ_{rr} for different directions through a spherical dot. The radius of the dot considered is 3nm and the center of the QD is the origin of the coordinate system used. The misfit strain is 6.7% and parameters for GaAs have been used. The solid line represents the isotropic model while the dotted dashed lines represent anisotropic models. Reproduced with permission from [93], Andreev et al., *J. Appl. Phys.* 86, 297 (1999). © 1999, American Institute of Physics.

Fig. 25. Values of anisotropy ratio $A(= 2C_{44}/(C_{11}-C_{12}))$ ranging from 0.25 to 4.0 were considered both for the QDs and the matrix. The ratios of the cap-layer thickness to dot height considered were 2.0, 3.0, 4.0, 5.0, and 6.0, respectively.

From Fig. 26, Pei et al. [122] noted that the value of ε_{xx} contour increases with A changing from 1.0 to 4.0 while it decreases with A changing from 1.0 to 0.25. Also, when $A > 1$, $[100]$ and $[\bar{1}00]$ are the “elastically soft” directions with the strain decaying rapidly in these directions. These same directions become the “elastically hard” directions when $A < 1$. For different values of A , ε_{xx} has a positive value in the matrix and increases from zero to a local maximum at the interface between the matrix and the wetting layer. In the QD region, it changes sign and its absolute value reduces till one reaches the interface between the QD and the capping layer. In the cap layer, ε_{xx} changes its sign again to being positive. Compressive strain increases significantly with increase in A from 0.25 to 4.0. The ε_{xx} profile is also significantly affected due to anisotropy considerations.

2.4.2. Nonlinear Effects

Generally, elastic material properties are assumed to be independent of strain. Ellaway and Faux [123] examined the accuracy of this assumption by investigating the behavior of elastic stiffnesses of InAs under uniform strain using atomistic methods. By using the three distortions as advised by Mehl [124–126] the three independent elastic stiffnesses C_{11} , C_{12} , and C_{44} , for a cubic crystal, were determined. Small distortions were applied to the crystal over a range of volumetric strains to evaluate the effective elastic stiffness at each strain level. For the atomistic simulation, Stillinger-Weber potentials [68] were employed using the parameters for InAs provided by Ichimura [127]. The elastic stiffnesses C_{11} and C_{12} increased with volumetric strain demonstrating that materials tend to become harder on being compressed. C_{44} was however found to hardly vary with volumetric strain [123]. Clearly, the strain dependence of elastic parameters renders the elastic boundary value problem nonlinear. After proper accounting for strain dependent elastic parameters, Ellaway and Faux [123] found significant difference in the hydrostatic strain calculation for a spherical InAs QD embedded in an GaAs matrix.

Ellway and Faux [128] also investigated the effect of volumetric strain on the degree of anisotropy and on the two-dimensional (biaxial) Poisson’s ratio. The anisotropy coefficient was found to have very weak dependence on the volumetric strain while the two-dimensional Poisson’s ratio was found to increase with pressure showing good agreement with the estimate provided by Frogley et al. [129–130]. Lepkowski and Majewski [131–132] investigated

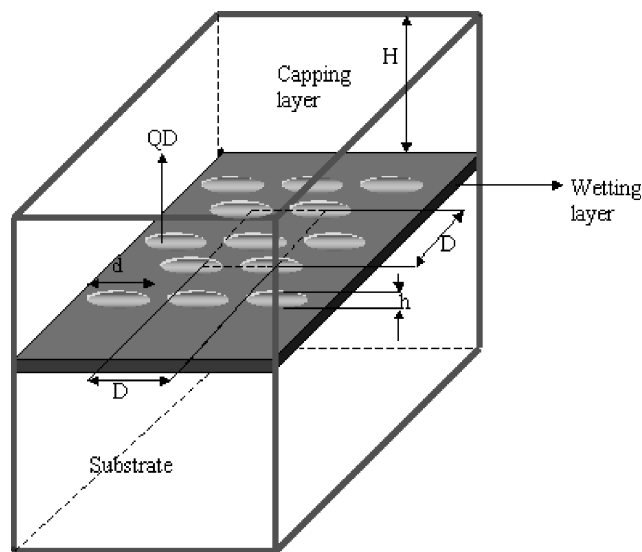


Figure 25. Schematic of an array of lens-shaped QDs. Distance (D) is 45 nm; thickness of the wetting layer (WL) is 1 nm. The base diameter (d) is 24 nm, while the height of the QD (h) is taken to be 6 nm. A lattice mismatch strain of 4% is assumed. Adapted from Pei et al. [122].

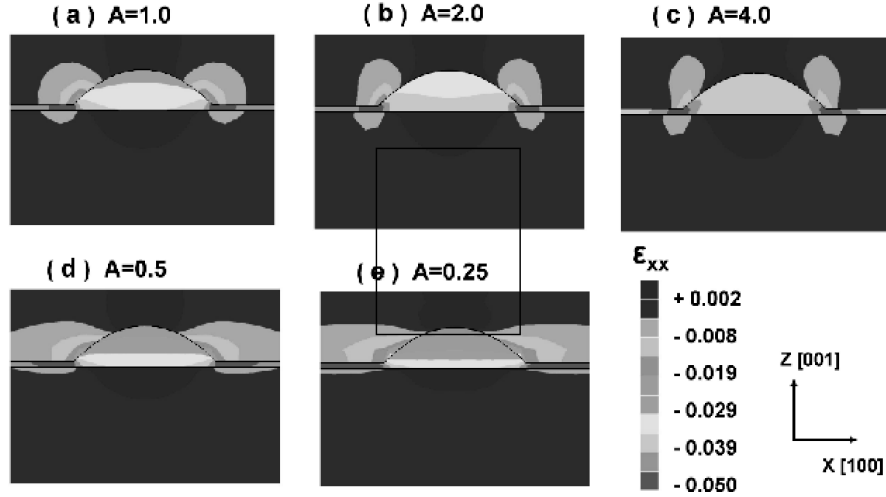


Figure 26. Contours in the midplane of one of the lens-shaped dots from Fig. 26 for different values of anisotropy ratio A . Reproduced with permission from [122], Pei et al., *J. Appl. Phys.* 93, 1487 (2003). © 2003, American Institute of Physics.

the pressure dependence of elastic constants in zinc-blende InN, GaN, and AlN using density functional formalism and demonstrated results similar to previous works discussed [123, 128].

2.5. Effect of Coupled Fields: Piezoelectricity

In addition to the coupling with the band structure, the stress arising out of a misfit quantum dot in a piezoelectric semiconductor material, additionally couples with the carriers through the piezoelectric effect. Like strain-band structure coupling, piezoelectric effect too can significantly alter the electronic and optical properties of semiconductor devices [22, 133–135].

2.5.1. Piezoelectric Effect Around a Spherical Dot

Once again, we consider first the simplest example: a spherical QD of radius, R , located in an infinite medium. The piezoelectric polarization, \mathbf{P} , induced by strain is given by

$$P_i = e_{ijk} \varepsilon_{jk} \quad (50)$$

where e_{ijk} is the piezoelectric tensor and ε_{jk} is the usual strain tensor.

$$\begin{aligned} e_{ijk} &= e_{14} \text{ for } \{ijk\} = \{123\} \text{ or permutations} \\ &= 0 \text{ otherwise} \end{aligned} \quad (51)$$

where e_{14} is the piezoelectric constant [136].

The polarization vanishes inside the spherical dot because the purely dilational strain present inside the sphere does not cause piezoelectric effect in a material with $\bar{4}3m$ symmetry. As a result there is no piezoelectric potential within a spherical quantum dot. For the region outside the dot, the polarization, \mathbf{P} , can be related to the charge density per unit volume, $\rho(\mathbf{r})$ as follows:

$$\rho(\mathbf{r}) = -\nabla \cdot \mathbf{P} \quad (52)$$

which when combined with Eqs. (50), (51), and (11), results in [54]

$$\rho(\mathbf{r}) = \frac{-270Ke_{14}}{3K + 4\mu} \varepsilon^m R^3 \frac{xyz}{r^7} \quad (53)$$

At the surface, the charge density σ is given by

$$\sigma = \mathbf{P} \cdot \hat{\mathbf{n}} \quad (54)$$

which can be written as

$$\sigma = 6e_{14} \left(\frac{9K}{3K + 4\mu} \right) \varepsilon^m \frac{xyz}{R^3} \quad (55)$$

Because of the polarization described by Eq. (54–55), the piezoelectric potential $\varphi(\mathbf{r})$ inside the dot can be written as [54]

$$\varphi(\mathbf{r}) = -\frac{3e_{14}\varepsilon^m R}{\varepsilon_0\varepsilon_r} \frac{9K}{3K + 4\mu} \left(\frac{R}{r} \right)^2 \left[1 - \left(\frac{R}{r} \right)^2 \right] \frac{xyz}{r^3} \quad (56)$$

where ε_r is the dielectric constant of the semiconductor and ε_0 is the dielectric constant of free space. The maximum potential occurs at, $r = a\sqrt{2}$. This potential would penetrate inside an inclusion possessing a less symmetric shape and one would expect it to shift the energy levels of electrons inside the dot. However, because of the presence of the extremely small length factor of R (the radius of the quantum dot) in Eq. (56), this potential tends to be very small and exercises little if any influence on the energies of electrons [54].

2.5.2. Piezoelectric Effect Around Any Dot

As highlighted by Davies [54], the elastic displacement, \mathbf{u} , in the presence of a lattice mismatch strain, can be described by a scalar potential χ in a manner similar to the electric field-elastic potential relationship:

$$\mathbf{u} = \nabla\chi \quad (57)$$

This potential obeys Poisson's equation:

$$\nabla^2\chi = \frac{9K}{3K + 4\mu} \varepsilon^m \quad (58)$$

Using the usual Green's function for the Laplace equation the following relationship can be obtained for χ , at a generic point in space [54],

$$\chi(\mathbf{r}) = -\frac{1}{4\pi} \frac{9K}{3K + 4\mu} \int \frac{\varepsilon^m(\mathbf{r}') d^3\mathbf{r}'}{|\mathbf{r} - \mathbf{r}'|} \quad (59)$$

The piezoelectric charge density is given in terms of χ by

$$\rho(\mathbf{r}) = -e_{ijk}\chi_{ijk} \quad (60)$$

We know that

$$\nabla^2\varphi(\mathbf{r}) = -\frac{\rho(\mathbf{r})}{\varepsilon_0\varepsilon_r} \quad (61)$$

Using Eqs. (61), (60), and (58), we have [54]

$$\nabla^4\varphi(\mathbf{r}) = \frac{9K}{3K + 4\mu} \left(\frac{e_{ijk}}{\varepsilon_0\varepsilon_r} \varepsilon(\mathbf{r})_{ijk}^m \right) \quad (62)$$

Davies has [100] defined a “piezoelectric pseudopotential” Φ such that

$$\nabla^2\Phi(\mathbf{r}) = \chi(\mathbf{r}) \quad (63)$$

From Eq. (51) we obtain

$$\nabla^4\Phi(\mathbf{r}) = \frac{9K}{3K + 4\mu} \varepsilon^m(\mathbf{r}) \quad (64)$$

thereby expressing φ in terms of Φ in a biharmonic equation. The piezoelectric potential can then be obtained after some further manipulation as a surface integral of the following form [100]:

$$\varphi(\mathbf{r}) = \frac{9e_{14}\varepsilon^m}{4\pi\epsilon_0\epsilon_r} \left(\frac{9K}{3K+4\mu} \right) \oint \frac{(x-x')(y-y')(z-z')(\mathbf{r}-\mathbf{r}') \cdot d\mathbf{S}'}{|\mathbf{r}-\mathbf{r}'|^5} \quad (65)$$

In the analytical models previously described (and some finite-element models notably [137]), the elastic field induced is first determined subject to given mechanical boundary conditions. The elastic solution is then used to estimate the polarization, which induces the electric potential and field. The electric field is then solved for by imposing purely piezoelectric boundary conditions. Such an approach is often called the “semi-coupled model”.

A fully coupled model was proposed by Pan [138] predicated on earlier works involving the determination of displacement Green’s functions in a fully coupled and generally anisotropic piezoelectric half space [139]. In a fully coupled model, the elastic stress field, σ_{ij} , and the electric displacement field, D_i , are coupled by the following constitutive relations:

$$\sigma_{ij} = C_{ijkl}\varepsilon_{kl} - e_{kji}E_k \quad (66a)$$

$$D_i = e_{ijk}\varepsilon_{jk} + \epsilon_{ij}E_j \quad (66b)$$

where ϵ_{ij} is the dielectric tensor and E_k is the electrical field. The strain ε_{ij} and the electric field E_i are related to the elastic displacement u_i and the electric potential ϕ by their corresponding constitutive relations.

Use of the Barnett-Lothe notation [140] allows one to recast Eqs. (66a) and (66b) into a unified single equation. For a finite-sized QD, Pan [138] then expressed the induced elastic and piezoelectric fields in terms of boundary integrals on the surface of the QD and the point-force/point-charge Green’s function solutions.

To facilitate comparison between the semi-coupled and the fully coupled model, Pan [138] presented the cases of GaAs and AlN quantum dots for both the infinite-space and half-space situations. Under the assumptions of elastic isotropy, analytical solutions have been arrived at, using the semi-coupled model in the full- and half-space GaAs and in the full-space AlN.

Some of the results of Pan [138] are now discussed. In his work, a lattice mismatch ε^m of 7% was assumed while modeling the quantum dot system for both GaAs and AlN. The quantum dots themselves are point spheres with an equivalent volume of $\frac{4}{3}\pi a^3$ ($a = 1$) nm and are located at the origin $\mathbf{r} = (0, 0, 0)$ for the full-space case and at $\mathbf{r} = (0, 0, h)$ ($h = 2$ nm) for the half space case; $z = 0$ being the free surface. The electromechanical coupling factor g for a piezoelectric material is defined as

$$g = \frac{e_{\max}}{\sqrt{\epsilon_{\max}/C_{\max}}} \quad (67)$$

where e_{\max} , ϵ_{\max} , and C_{\max} are the maximum absolute values of the piezoelectric coefficients, dielectric constants, and elastic constants. For the specific case of GaAs, with a weak electromechanical coupling ($g = 0.04$), the semicoupled model was found by Pan [138] to yield results similar to the fully coupled model for the elastic and piezoelectric fields (for full- and half-space). However, in the case of AlN, which has a rather strong electromechanical coupling ($g = 0.32$ opposed to 0.04 for GaAs), the semicoupled model rendered substantially different results from the fully coupled model. This is well illustrated in Fig. 27, where both fully coupled and semicoupled models predict nearly identical electric fields in the case of the GaAs, while significant differences are observed between the two-models while estimating the electric-field for the AlN case [138]. In fact at $r = (1, 1, 1)$ nm, the electric field predicted by the semi-coupled model in the GaAs case falls short of that predicted by the fully coupled model by nearly a factor of 2.

On a related note, Pan in a subsequent work [141] applied the three-dimensional Green’s function solution based on the fully coupled model to four substrates, namely, GaAs (001), GaAs (111), Iso (001), and Iso (111) to show that the isotropic model fails to predict the induced elastic and piezoelectric fields for piezoelectric semiconductors. The elastic constants

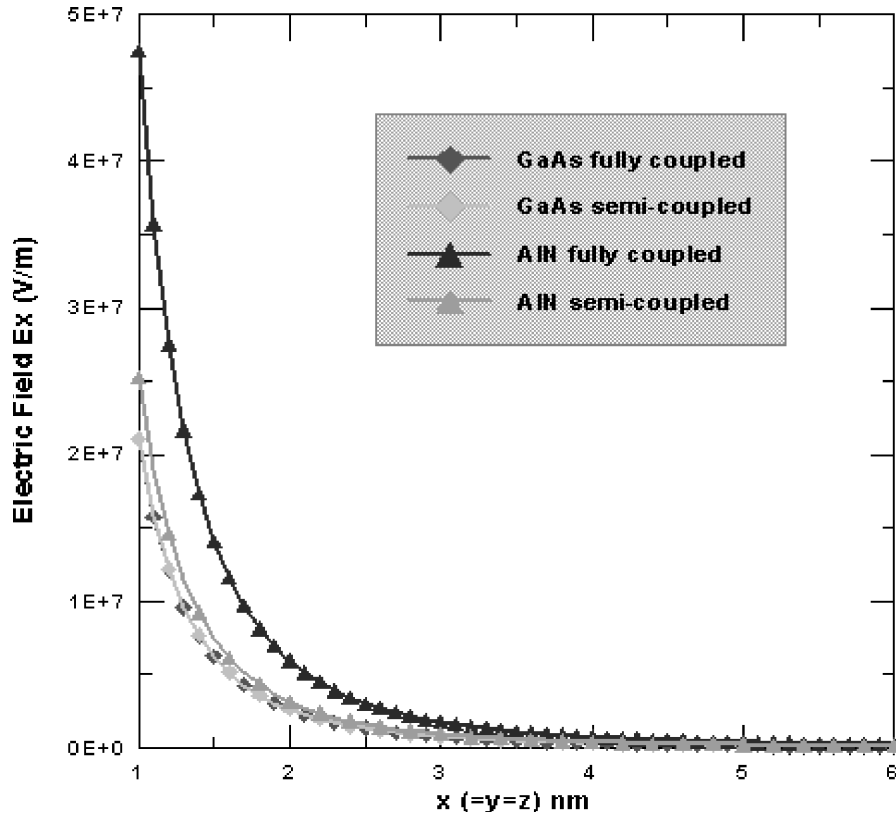


Figure 27. A comparison between the electric-field E_x predicted by the semi-coupled and fully coupled models for two different quantum dot systems (a) AlN and (b) GaAs in infinite space. The dot is point spherical with an equivalent radius of $a = 1$ nm and is located at $r = (0, 0, 0)$. The variation in the above diagram is traced along $r = (x, x, x)$. Reproduced with permission from [138], E. Pan, *J. Appl. Phys.* 91, 3785 (2002), Fig. 3. © 2002, American Institute of Physics.

for Iso (001) and Iso (111) were assumed to be isotropic. The elastic and piezoelectric fields on the surface of these substrates, due to a buried point quantum dot with an initial dilational misfit strain, were also studied (Figs. [28]–[30]). In the examples that Pan illustrates, the QD is a point sphere buried at a depth h ($h = 10$ nm), with an equivalent radius of a ($a = 3$ nm); an initial mismatch strain of $\varepsilon^m = 7\%$ is assumed.

From Fig. 28, as Pan [141] noted, it is clear that the isotropic model is clearly not suitable to estimate the elastic fields in anisotropic GaAs. While the isotropic hydrostatic strain has complete rotational symmetry about the z -axis, GaAs (001) displays a C_4 symmetry and GaAs (111) exhibits a C_3 symmetry. The values of strain relaxation achieved at the surface for the three cases are also markedly different with high-hydrostatic strain prevailing in the GaAs (111) case (10% of misfit strain in the GaAs (111) case as against 7% and 3% for Iso (001) and GaAs (001), respectively).

For similarly orientated GaAs and Iso semiconductors (for example, GaAs (001) or (111) and Iso (001) or (111), respectively), Pan [141] have reported some similarities between the contours of piezoelectric potential (Fig. 29) (even the horizontal electric field has been demonstrated to display the said similarities) at the surface. However, as Fig. 30 show, the vertical electric field E_z , at the surface in GaAs (001) or (111) does not exhibit any similarity to the isotropic case. Pan [141], therefore, have suggested use of caution while applying the isotropic assumption to the GaAs semiconductor case to avoid arriving at erroneous results.

2.6. Effect of Size

As evident so far in our review, generally speaking, researchers have used the well established continuum elasticity theory (both numerically and analytically) to estimate mechanical strains. Those then are coupled to some suitable band-structure calculation method (such

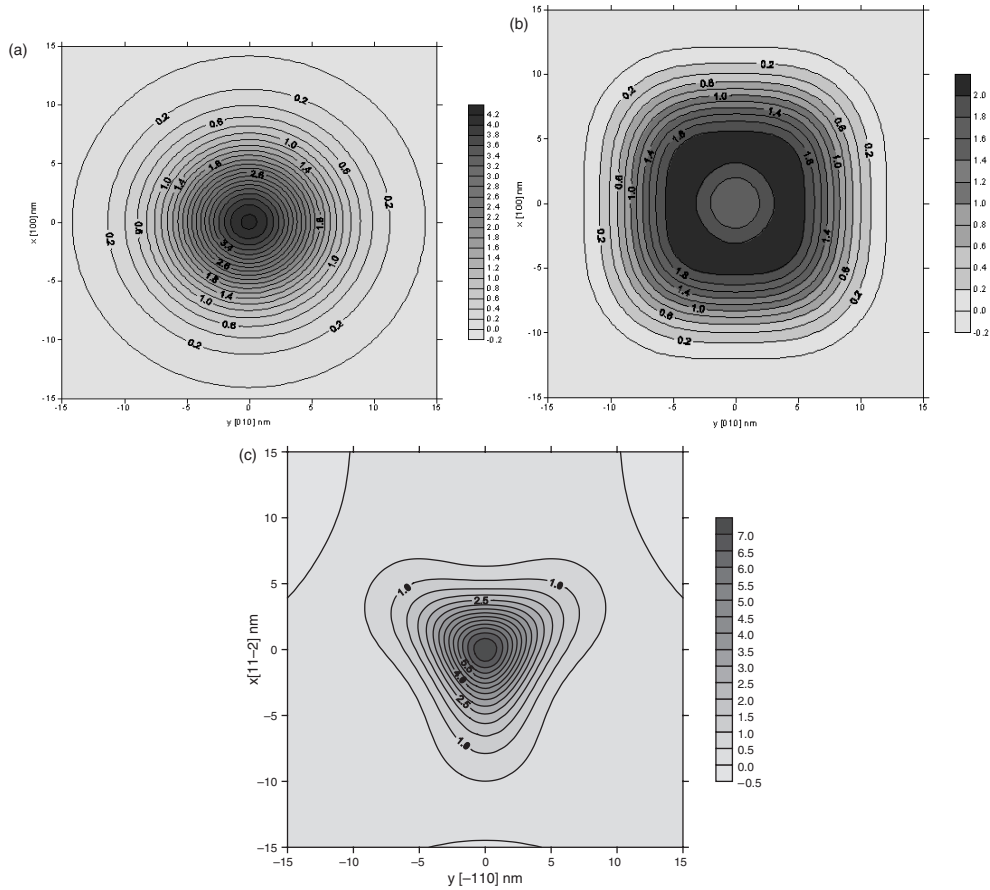


Figure 28. Contours of ε_{ii} (10^{-3}), the hydrostatic strain due to a point QD of volume $v_a = 4\pi a^3/3$ buried at a depth of $h = 10$ nm, (a) on the surface of the isotropic crystal (the contours are similar for Iso(001) and Iso(111)); (b) on the surface of GaAs(001); (c) on the surface of GaAs (111). Reproduced with permission from [141], Pan, *J. Appl. Phys.* 91, 6379 (2002), Fig. 2(a-c). © 2002, American Institute of Physics. These figures clearly indicate that the isotropy model is not suitable to determine strain distributions in anisotropic GaAs semiconductor. Other elasticity fields (like stress and displacement) show similar variation to the strain shown in the diagram.

as tight binding or the **k,p** approach) to estimate the impact of strain on the optoelectronic properties. Classical continuum mechanics, is however, intrinsically size independent. This is in contradiction to the physical fact that at the size-scale of a few nanometers, deformations and elastic state are size dependent and a qualitative departure from classical mechanics is

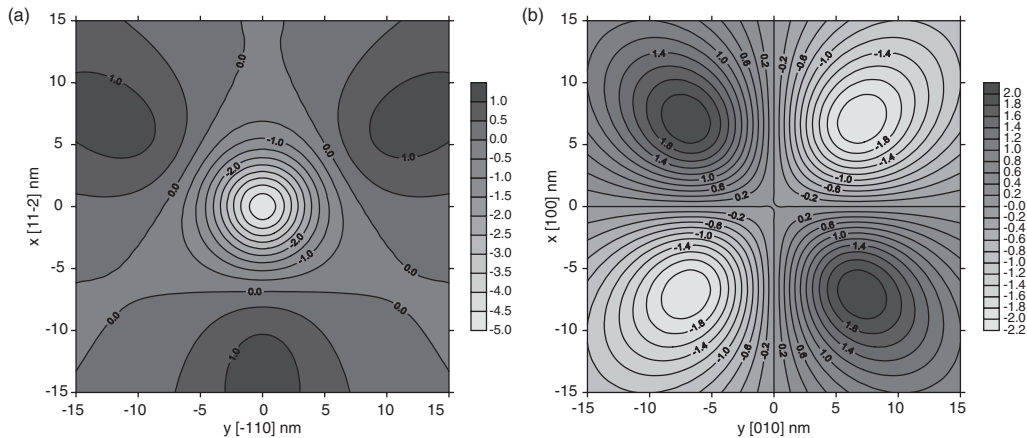


Figure 29. Contours of piezoelectric potential due to a point quantum dot of volume $v_a = 4\pi a^3/3$, and buried under a depth $h = 10$ nm; (a) at the surface of GaAs (111); (b) at the surface of GaAs (001). Reproduced with permission from [141], Pan, *J. Appl. Phys.* 91, 6379 (2002), Fig. 3(a-b). © 2002, American Institute of Physics.

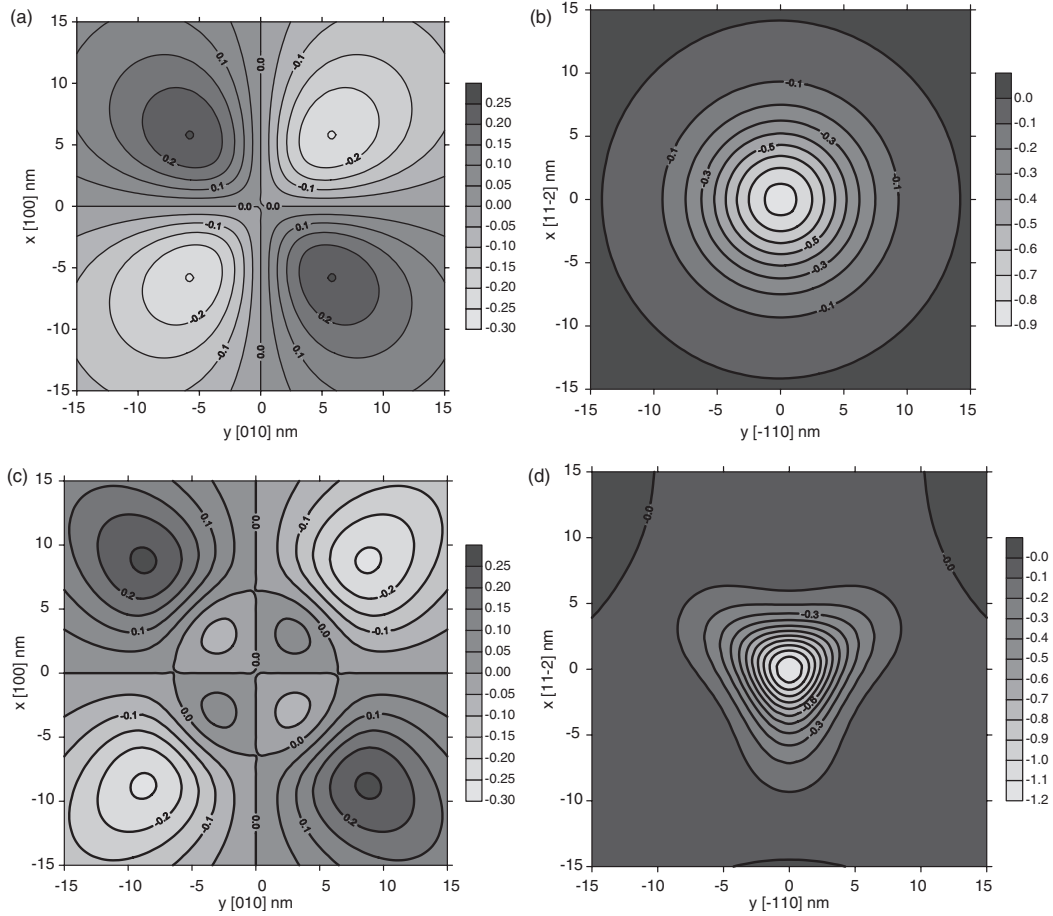


Figure 30. Contours of vertical electric field E_z ($10^7 V/m$) due to a point quantum dot of volume $v_a = 4\pi a^3/3$ and buried under a depth $h = 10$ nm; (a) at the surface of Iso (001); (b) at the surface of Iso (111); (c) at the surface of GaAs (001); (d) at the surface of GaAs (111). Reproduced with permission from [141], Pan, *J. Appl. Phys.* 91, 6379 (2002). Fig. 5(a–d). © 2002, American Institute of Physics.

expected. The obvious alternative method to compute strain is the use of atomistic simulations. Nevertheless, a field theoretic method is highly desirable (in the same vein several of the models discussed so far) albeit that does also account for the scaling or size effects in strain likely to be prevalent at these small length scales.

There are chiefly two physical mechanisms that may alter continuum elasticity predictions and result in scaling or size effects in the strain calculations in quantum dots: (1) surface or interfacial energy effects and (2) nonlocal elastic interactions. Both are likely to be small and only of importance for exceedingly small quantum dots, nevertheless these effects can be important in certain cases.

2.6.1. Surface/interface Energy Effects

For structures with sizes > 50 nm, typically, the surface-to-volume ratio is negligible and the deformation behavior is governed by classical volume strain energy. However, at submicron-length scales the properties of the quantum dot surface/interface are expected to play a role in the determination of its elastic state. Simply from dimensional considerations we expect that strain should scale $\sim 1/R$ (where R is some characteristic length of the quantum dot and that the proportionality constant is related to surface or interface energy). In the context of quantum dots and embedded inclusions, this effect has been discussed in some recent publications by one of the authors [142–144]. The latter works, presented the size-dependent elastic state of QDs based on the involvement of surface/interfacial energies at the nanoscale. For example, errors in strain calculation as high as 12% were reported in the determination of hydrostatic strain in a buried spherical QD (in the size range of 2 nm).

Surface elastic effects have been considered by a variety of authors in various contexts, for example, nanostructures [145], nanocomposites, thin films [146], surface steps [147–148], quantum dots, and so forth. The reader is referred to the following review articles and references therein for comprehensive details. From the point of view of a mechanics, Gurtin and Murdoch [149], Murdoch [150], and Gurtin et al. [151] appear to have established a fairly rigorous framework to incorporate surface or interface energies which is what we following in the present article to tackle the quantum dot strain scaling problem.

Consider an arbitrary shaped smooth interface between an embedded inclusion and surrounding host matrix, characterized by a unit normal \mathbf{n} . Let this interface be “attached” to the bulk (i.e., both inclusion and matrix) without slipping or any other discontinuity of displacements across it. This implies that we consider only a coherent interface. In contrast to the classical case where surface energies are neglected, we now require that the interface of the inclusion and the matrix be endowed with a deformation dependent interfacial energy, Γ . The interfacial or surface energy is positive definite. This quantity is distinct from the bulk deformation dependent energy due to the different coordination number of the surface/interface atoms, different bond lengths, angles, and a different charge distribution [152]. Within the assumptions of infinitesimal deformations and a continuum field theory, the concept of surface stress and surface tension can be clarified by the (assumed *linearized*) relation between the interface/surface stress tensor, $\boldsymbol{\sigma}^s$, and the deformation dependent surface energy, $\Gamma(\boldsymbol{\varepsilon}^s)$:

$$\boldsymbol{\sigma}^s = \tau_o \mathbf{P}^s + \frac{\partial \Gamma}{\partial \boldsymbol{\varepsilon}^s} \quad (68)$$

Where applicable, superscripts B and S indicate bulk and surface, respectively. Here, $\boldsymbol{\varepsilon}^s$ is the strain tensor for surfaces that will result from the projection of the conventional bulk strain tensor on to the tangent plane of the surface or interface, while τ_o is the deformation independent surface/interfacial tension. The surface projection tensor, \mathbf{P}^s which maps tensor fields from bulk to surface and vice versa is defined as:

$$\mathbf{P}^s = \mathbf{I} - \mathbf{n} \otimes \mathbf{n} \quad (69)$$

Consider an arbitrary vector \mathbf{v} . The surface gradient and surface divergence, then, take the following form [151]:

$$\begin{aligned} \nabla_s \mathbf{v} &= \nabla \mathbf{v} \mathbf{P}^s \\ \text{div}_s(\mathbf{v}) &= \text{Tr}(\nabla_s \mathbf{v}) \end{aligned} \quad (70)$$

Here, we have also defined the surface gradient operator (∇_s) and the surface divergence, which we shall shortly employ. We repeat here the equilibrium and isotropic constitutive equations of bulk elasticity:

$$\begin{aligned} \text{div } \boldsymbol{\sigma}^B &= 0 \\ \boldsymbol{\sigma}^B &= \lambda \mathbf{I}^3 \text{Tr}(\boldsymbol{\varepsilon}) + 2\mu \boldsymbol{\varepsilon} \end{aligned} \quad (71)$$

At the interface, the concept of surface or interface elasticity [149, 151] is introduced, which is excluded in the classical elasticity formulation:

$$\begin{aligned} [\boldsymbol{\sigma}^B \cdot \mathbf{n}] + \text{div}_s \boldsymbol{\sigma}^S &= 0 \\ \boldsymbol{\sigma}^S &= \tau_o \mathbf{P}^s + 2(\mu^s - \tau_o) \boldsymbol{\varepsilon}^S + (\lambda^s + \tau_o) \text{Tr}(\boldsymbol{\varepsilon}^S) \mathbf{P}^s \end{aligned} \quad (72)$$

Isotropic interfaces or surfaces can be characterized by surface Lamé constants λ^s , μ^s , and surface tension, τ_o . The square brackets indicate a jump of the field quantities across the interface. Only certain strain components appear within the constitutive law for surfaces due to the 2×2 nature of the surface stress tensor (i.e., only the tangential projection of the strains on the interface are included consequently, $\mathbf{P}^s \cdot \mathbf{n} = 0$). In absence of surface terms, Eq. (72) reduce to the usual normal traction continuity equations of classical elasticity.

Thus, while the infinitesimal strain tensor in the bulk (both inclusion and matrix) is defined as usual, the surface strains involve the use of projection tensor (Eq. 69).

$$\boldsymbol{\varepsilon}^s = \frac{1}{2}(\mathbf{P}^s \nabla_s u + \nabla_s u^T \mathbf{P}^s) \quad (73)$$

Implicit in Eq. (73) is our assumption of a coherent interface. Using these basic equations, Sharma and Ganti [144, 153–155] have explicitly derived the dilatation strains for embedded quantum dots. To be more explicit, the dilatational strain in an isotropic spherical lattice mismatched embedded quantum dot that correctly incorporates size effect due to interfacial energies can be written as:

$$\text{Tr}(\boldsymbol{\varepsilon}) = 3 \frac{3K\varepsilon^m - 2\tau_o/R}{4\mu + 3K + 2K^s/R} \quad (74)$$

where K_s is the surface elastic modulus defined as $2(\lambda^s + \mu^s)$. Note that for large radius of QD ($R \rightarrow \infty$) or zero surface energy, the result reverts to the classical solution used by several authors (see, e.g., Yang et al. [23]). Equation (74), of course implies that, even if the QD is not embedded, there is a finite strain (which of course is very small except in the smallest possible QDs):

$$\text{Tr}(\boldsymbol{\varepsilon}) = -\frac{3}{3K_{\text{QD}} + 2K_s/R} \left(\frac{2\tau_o}{R} \right) \quad (75)$$

In a collaborative work, one of the authors presented numerical density function theory (DFT) simulations of Si clusters that illustrated the impact of surface energy induced strains (Peng et al. [156]). *Ab initio* simulations of quantum dots, for the purpose of ascertaining scaling laws associated with their optoelectronic properties, have also been carried out by other researchers [157–158]. These previous works, however, did not notice the aforementioned additional scaling effects since they (as is often done conventionally) constrained the surface atoms to remain configurationally fixed thus effectively precluding the manifestation of influence of surface energies on strain. In the simplest possible picture, for the case of unembedded quantum dots where there is no apparent source of strain (i.e., no lattice mismatch), the effect of surface tension is excluded (see Eq. [75]). In the case of embedded quantum dots, the correction to the lattice mismatch-induced strain due to interfacial tension and elasticity is excluded. This form of simulations, where surface atoms are not allowed to relax, is primarily employed for savings in computational time with the unfortunate consequence of effectively voiding the strain-induced scaling. For example, the DFT computation time for a surface relaxed cluster $\text{Si}_{59}\text{H}_{60}$ is 1,694 minutes, while the time for the same cluster without atomic relaxation is 125 minutes.

We now proceed to present a test of the assertions and implications of Eq. (75) through DFT calculations of unembedded Si clusters of various sizes. We note here the work of Delley [159] who performed such a study without incorporating the surface effects outlined in Eq. (75). The surface atoms were configurationally fixed in his analysis, thus excluding the scaling effect we predict. To retain the tetrahedral configuration of silicon (refer to Fig. 31), all the dangling bonds of the surface silicon atoms were terminated by hydrogen at initial bond length of 1.47 Å. The clusters were varied from Si_5H_{12} to $\text{Si}_{239}\text{H}_{196}$ (i.e., from 5.8 to 21.0 Å).

The surface atoms were allowed to relax to their equilibrium state thus triggering the strain in Eq. (75). The main results are depicted in Fig. (32), where the band gap is plotted as a function of cluster size and compared with Delley's [159] unrelaxed cluster study. As already anticipated, we note a significant shift in band gap at small sizes where surface energy-induced strains make their presence felt. A somewhat surprising result that emerges from Fig. (32) is that this scaling effect disappears for extremely small sizes!

A maximum band-gap shift of nearly 0.51 eV is observed at a cluster size of 17 atoms. Plausible explanations for the disappearance of this new scaling effect at sizes below 17 atoms appear to suggest that surface energy parameterized by surface tension and surface

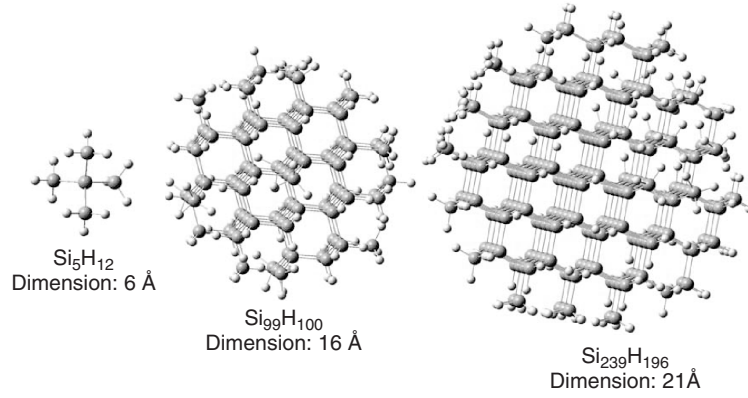


Figure 31. Snapshots of various-sized Si clusters used in the DFT simulations.

elastic modulus must itself be size dependent, that is,

$$\{\tau_o, K_s\} \propto \frac{\{\tau_o, K_s\} \text{ at "large" size}}{1 + k/R} \quad (76)$$

where k is a constant. Obviously, as $R \rightarrow 0$, the surface energy smoothly vanishes, explaining the disappearance of concerned scaling effect at extremely small sizes. Physically and in hindsight this is easy to justify. The continuum field concept of surface energy, tension, and surface elastic modulus signifies the difference between the surface atom properties with the corresponding ones in the bulk (due to different coordination number, charge distribution, bond length, etc.; a mismatch strain of 3.5% and $K \sim 100$ Gpa and $\mu \sim 60$ Gpa. However, at extremely small sizes, where only few atoms remain, this difference and the distinction between surface and bulk atoms becomes very tenuous or, in other words, the continuum notions of surface energy (if one insists on using them) must become zero.

2.6.2. Nonlocal Effects

Nonlocal interactions are another mechanism that is only of importance when the quantum dot size is comparable to the lattice parameter. At small length scales (approaching a few nanometers comparable to the discrete structure of matter) the implicit long-wavelength assumption of classical elasticity breaks down. This break down is caused partially by the long-range interactions between atoms, which are inadequately represented by classical elasticity. As one would expect, several phenomena at the level of a few lattice spacing are inadequately captured by classical elasticity and researchers often see enriched continuum

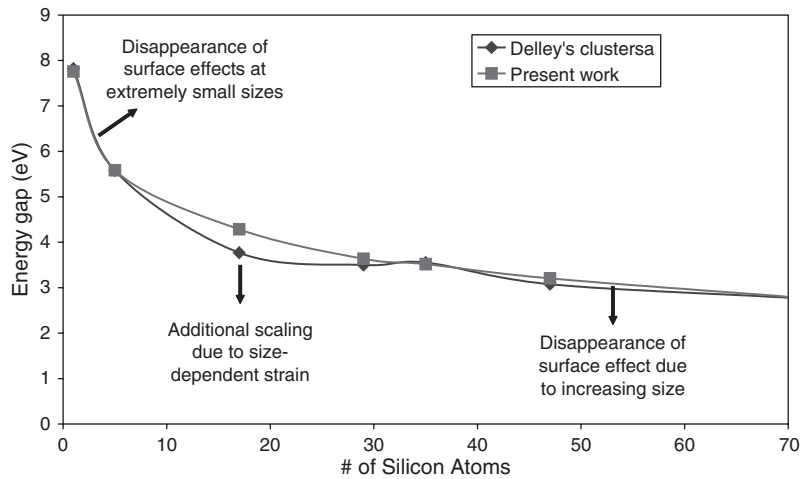


Figure 32. Comparison of the present work incorporating the size-dependent strain due to surfaces and Delley's [159] results. Adapted from Peng et al. [156].

theories such as nonlocal elasticity as a replacement for atomistic simulations (or, alternatively, a bridge between atomistic and conventional continuum mechanics). For example, the ubiquitous singularities ahead of crack tips and dislocation cores (as predicted by classical mechanics) are indeed a break down of traditional elasticity at short wavelengths [157]. One possible means to circumvent the long wavelength assumption of classical elasticity is to invoke higher order gradients in the elastic energy expansion. In a recent work [160], one of the authors derived the complete Eshelby's tensor for an embedded quantum dot.

Consider the classical isotropic elastic material. The strain energy function is quadratic in strains:

$$W(x) = \mu \varepsilon_{ij} \varepsilon_{ij} + \frac{1}{2} \lambda \varepsilon_{kk}^2 \quad (77)$$

Here, ε is the usual strain tensor related to \mathbf{u} (displacement vector) as $\text{sym}(\nabla \mathbf{u})$, and $[\bullet]_j$, and ∂_j will be used interchangeably to indicate differentiation with respect to spatial variable x_j . Note that the antisymmetric part of the deformation gradient that is, ω ($= \text{asym } \nabla \mathbf{u}$) is absent from Eq. (77) because the quadratic term in ω is not rotationally invariant—a necessary requirement for the energy function in Eq. (77). For small quantum dot sizes, additional gradient terms (absent in Eq. [77]) may also contribute and are considered to phenomenologically representative of nonlocal interactions [157–158]. The latter is achieved by suitably adding higher-order terms containing gradients of strain and rotation. (Indeed, the gradients of ω are admissible because those fields are invariant with respect to the Euclidean group of transformations $\text{SO}(3) \triangleright \text{T}(3)$ unlike ω itself.) The general form of the elastic energy involving first gradients of strain and rotation is

$$W(x) = W(\partial_i u_j, \partial_l u_l, \partial_i \partial_l u_l, \partial_i \partial_l u_i) \quad (78)$$

In the isotropic case, the energy density that is invariant to $\text{SO}(3) \triangleright \text{T}(3)$ group then takes the form [158]

$$\begin{aligned} W(x) = & \frac{\mu}{2} (\partial_i u_j)^2 + \frac{\mu + \lambda}{2} (\partial_l u_l)^2 + \frac{2\mu + \lambda}{2} l^2 \partial_i \partial_l u_l \partial_i \partial_j u_j \\ & + \frac{\mu l^2}{2} (\partial_l^2 u_i \partial_l^2 u_i - \partial_i \partial_l u_l \partial_i \partial_j u_j) \end{aligned} \quad (79)$$

Two new coupling constants (in addition to the Lamé parameters) now appear namely l' and l . Both have units of length. For band-gap calculations in quantum dots, one typically requires only the dilatation and in the isotropic case (as it turns out), the last term in Eq. (79) plays no role, and hence, in the following, we set $l = 0$. Further, using a variational argument (by appealing to the Euler-Lagrange equations), the governing field equation can be derived as well as the response quantities (i.e., “stresses”). The single Navier-like equation that emerges is

$$-\mu \partial^2 u_i - (\mu + \lambda) \partial_i \partial_l u_l + \underbrace{(2\mu + \lambda) l'^2 \nabla^2 \partial_i \partial_l u_l}_{\text{extra terms}} = 3K \delta_{ik} \partial_k [\varepsilon^m H(x)] \quad (80)$$

The underlined portion of Eq. (80) indicates the extra terms absent in *size-independent* classical elasticity. Zhang and Sharma [160] have derived the solution to the problem in Eq. (80) for the case of a misfitting spherical quantum dot. They obtain:

$$tr(\varepsilon) = \begin{cases} \frac{9K \varepsilon^m}{3K + 4\mu} \left[1 - (l' + R) e^{-R/l'} \frac{1}{l'} \frac{\sinh r/l'}{r/l'} \right] & r \in \Omega \\ \frac{9K \varepsilon^m}{3K + 4\mu} \left(R \cosh \frac{R}{l'} - l' \sinh \frac{R}{l'} \right) \frac{1}{l'} \frac{e^{-r/l'}}{r/l'} & r \notin \Omega \end{cases} \quad (81)$$

In Fig. 33, the normalized dilations strain as a function of position, various inclusion sizes and nonlocal coupling constant l' are plotted. The location $x/R = 1$ indicates the boundary of the spherical quantum dot. The size effect of the nonlocal solution is manifest. We note that, unlike both the classical and interfacial energy-based solution, the dilation incorporating

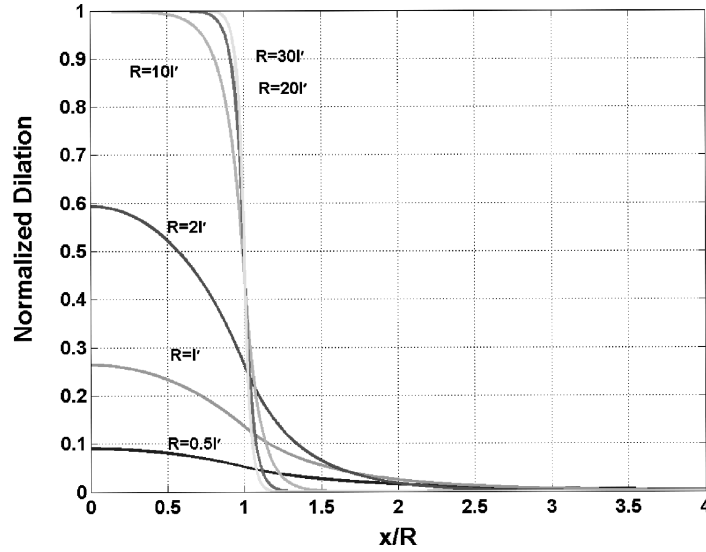


Figure 33. Strain dilatation as a function of position and size. The flat line with abscissa = 1 for $x/R < 1$ and = 0 for $x/R > 1$ represents the classical size-independent solution. Adapted from Zhang and Sharma [160].

nonlocal effects is inhomogeneous within the inclusion. Asymptotically, the nonlocal results converge to that of classical elasticity for large quantum dot size. Further, note that while the classical results predict the well-known zero dilatation outside the spherical quantum dot, in the case of nonlocal results we observe a small nonzero dilatation. Conforming to physical intuition, artificial jumps in stresses are removed in nonlocal results and the strains vary smoothly across the interface (or in other words the “continuum” sharp interface of the quantum dot/matrix acquires a “diffuse boundary layer” to the order of the characteristic length scale parameter.

To emphasize on the size dependency of our solution, the dilatation as a function of size (for a fixed position, i.e., $r = 0$) is also plotted in Fig. 34. We observe that while for large quantum dot size, roughly, $R > 7l'$, the nonlocal/strain gradient solution is indistinguishable from the classical one, the dilatation decreases significantly below this threshold and exhibits a marked departure from classical solution.

We now proceed to draw a comparison between surface energy effects (discussed in Eq. [74]) and nonlocal results. Unfortunately, while the nonlocal results can be adequately

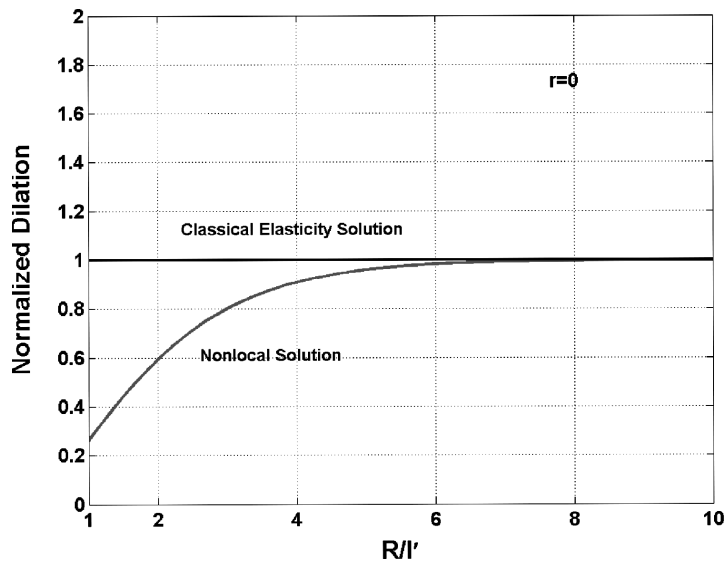


Figure 34. Dilatational strain as a function of size for fixed position ($r = 0$). The results are normalized with respect to classical elasticity solution. Adapted from Zhang and Sharma [160].

normalized (i.e., independent of mismatch strain), the surface/interfacial results cannot and are highly material dependent (both on the actual values of interfacial energy parameters as well as elastic moduli). We provide some general estimates here. The nonlocal coupling constant l' roughly corresponds to the lattice parameter of the quantum dot which is around ~ 0.4 nm for most materials. For the specific case of GaAs, in a rather interesting work, DiVincenzo [161] has determined the higher-order constants for the nonlocal elasticity theory. For the particular case of GaAs, we deduce l' to be ~ 0.82 nm (which, in fact, is much larger than the lattice parameter). So, for the purposes of general comparisons, it is safe to adopt l' to be roughly \sim lattice parameter. The interfacial tension (for coherent systems) is roughly to the order of ~ 1 J/m². Because (unlike both the classical and surface energy based result) the nonlocal solution is nonuniform, we compare results at the quantum dot center ($r = 0$). For diameters of {2, 4, 6, 8, 10} nm, respectively, the nonlocal deviation from classical elasticity result is {22, 2.2, 0.18, 0.014, ~ 0 }%, while we obtain a deviation of {19, 9.5, 6.3, 4.8, 3.8}% for interfacial energy-based results. Because of the exponential decay in the nonlocal solution (with respect to size), these effects decay far more rapidly than the interfacial effects but are likely to dominate for very small sizes (which though for most materials may be impossibly small and would be irrelevant anyway as we do not expect nonlocal theory to work for sizes smaller than $2l'$ —classical elasticity is expected to breakdown at even larger sizes, roughly, $6l'$).

2.7. Some Results from Inclusion Theory Useful for Strain Calculations in Quantum Dot Structures

Since the original appearance of Eshelby's paper [30] several works have extended, modified, and applied the concept of Eshelby's tensor to a diverse set of physical problems. We provide a brief review of this body of literature here in the hope that researchers addressing quantum dots may find them of use.

1. **Bonding conditions of inclusion.** The original assumption in Eshelby's work is that the inclusion is perfectly bonded to the matrix; that is, the normal tractions are continuous and so are the displacements. All works on quantum dots (that the present authors are aware of) make this same assumption, that is, matrix-quantum dot interface is perfectly bonded. Under certain conditions these conditions must be relaxed: jumps in displacement or tractions may be allowed. Various researchers have considered the imperfectly bonded inclusion, for example, Furuhashi et al. [167], Ru and Schiavone [168], Zhong and Meguid [169], Qu [170–171], and Kouris et al. [148]. Of course, physically, imperfectly bonded quantum dots will correspond to the case where defects are present at the interface. It is quite unclear whether then it is worthwhile to investigate the strain state in such dislocated quantum dots since most likely in comparison the mere presence of defects will overwhelm the electronic effects.
2. **Coated inclusions.** Frequently for technological reasons inclusions are embedded in a matrix with a coating (or which may be developed due chemical interaction with the matrix). A few representative works in this area are: Walpole [172], Luo and Weng [173], and Cherkaoui et al. [174], among many others. This scenario is very realistic especially in multialloy quantum dots where the outer rim of a quantum dot may be preferentially rich in one phase.
3. **Nonuniform mismatch strains.** Sendekyj [175] and Moschovidis [176] considered general polynomial transformation strain thus nonuniform lattice mismatch or thermal expansion strains can be mimicked. Their work is also useful for taking into account interactions between inhomogeneities. Asaro and Barnett [178] and Mura and Kinoshita [179] addressed polynomial eigenstrains in an anisotropic media. Note also must be made of the recent work of Rahman [180] who presents simplified calculations of Eshelby type tensors for polynomial eigenstrains.
4. **Enriched elasticity.** The classical theory of elasticity itself has been modified in several ways. Micromorphic elasticity takes into account additional micro-degrees of freedom such as independent rotations, dilations and shears. An extensive account of these theories can be found in Eringen [181]. As far as inclusion problems are concerned, it

appears that the only two solutions that exist are due to Cheng and He [182–183] who, respectively, solve the spherical and cylindrical inclusion problem. On the basis of the latter work, Sharma and Dasgupta [184] have formulated the overall properties of micropolar composites. Another enrichment of elasticity is whereby nonlocal interactions are introduced. Again, an up-to-date survey is given by Eringen [157]. A popular version of nonlocal elasticity is the strain gradient theory. Zhang and Sharma [160] have recently provided solutions of embedded inclusions in the strain gradient elasticity formalism.

5. **Inclusion-inclusion interactions.** As already noted above, the work of Moschovidis [176] provides an interesting discussion on interactions between two inclusions. Rodin and Hwang [177] provide a nice analysis of this problem and also contain several useful references. Interestingly, two dilating inclusions (same properties as matrix) have zero interaction energy in the isotropic limit. This is somewhat obvious since the external dilation in the isotropic case for all inclusion shapes is zero. Hence, if we are to use some of the isotropic results on quantum dots for dot–dot interaction, we may conclude that an interaction is absent. Anisotropy or half-space solution must be invoked to correctly account for this interaction. Interestingly, because the external dilation is nonzero in nonlocal elasticity (see Zhang and Sharma [160]), a finite interaction between dots should exist even in the isotropic case. However, this interaction is likely to be weak and only of importance for dots very closely spaced to each other. This issue requires further investigation.
6. **Anisotropy and shape.** Several works have modified Eshelby's (originally isotropic) formulation to incorporate anisotropic behavior. Progress has largely been made only in the plane case. An excellent, but somewhat dated, account of these aspects is given in the now classic monograph by Mura [35]. Some more recent works, that also contain an extensive list of references on this subject are Ru [162] who discusses arbitrary-shaped inclusions in anisotropic half and full plane, Li and Dunn [163] address coupled field anisotropic inclusion problems, and Pan and Yang [164] who present a semianalytical method for application to embedded quantum dots. Inclusion shapes: Chiu [50] has considered parallelepiped inclusion. Rodin [165] considers the general polyhedral inclusion and provides an elegant algorithmic approach to determine the elastic state of arbitrary polyhedral. So do Nozaki and Taya [166].

In addition to the aforementioned group of papers, several other works exist in the context of nonlinear behavior and of course in application areas (such as effective medium theories, phase transformations, stability among others). A review of those works is beyond the scope of this chapter. The following monographs, review articles, books, and references therein are recommended for the interested reader: Mura [35], Nemat-Nasser and Hori [33], Markov and Preziosi [185], Weng et al. [186], Bilby et al. [187], Mura et al. [188], and Mura [189].

3. SUMMARY AND OPEN ISSUES

In conclusion, we have reviewed and discussed several works and issues in calculation of strains in quantum dots and wires under myriad contexts of shape effects, presence of a free surface, anisotropy considerations, nonlinear effects, and presence of coupled effects (piezoelectricity). We have also provided a discussion on some of the novel size-dependent effects that may manifest themselves at the length scales at which these nanostructures exist.

Several avenues of research remain open and inadequately addressed. We highlight some of our own personal perspectives here.

Size effects in quantum dots appear to be the least explored. The use of classical continuum mechanics for strain calculations is typical which of course is size independent. As mentioned in the preceding Section 2.6.1 (in the context of surface energy effects), if care is not taken, even the atomistic studies may inadvertently exclude or underemphasize size effects. Some rather interesting scenarios are possible here. For example, we also discussed the size effects arising out of nonlocal interactions in a previous section. In such a theory, a characteristic length scale appears that is roughly in the neighborhood of the lattice parameter, that is, size effects in strain may become appreciable for dots that are close in

size to the lattice parameter. Obviously, this effect is small and only applicable for very tiny dots. In a recent work, Drugan and Willis [192] show that material with multiple inclusions behaves as a nonlocal solid with a characteristic length that may be much larger than the lattice parameter (and roughly scales with the inclusion size)! This implies that an array of quantum dots (depending upon the volume fraction or density) may cause a screening effect inducing nonlocal and hence noticeable size effects. This notion, apart from clarifying size effects, may also be a valuable tool in modeling the many body strain effects.

The discussion of possible screening effects of arrays of quantum dots on the scaling of strain leads to another relatively less studied topic: quantum dot–quantum dot interaction. In the isotropic limit, two dilating quantum dots in an infinite medium do not interact mechanically. Perhaps this has led many to conclude that strain-mediated interactions between quantum dots are of relatively less importance. There are, however, several exceptions to this notion. If quantum dots are sufficiently close to a free surface or interface, they will interact even in the isotropic limit through their image forces. Of course, proper accounting for the typically cubic anisotropy of most quantum dot materials will also remove this isotropic degenerate behavior. In particular, we note that the nonlocal solution of a single quantum dot exhibited nonzero dilation in the barrier. This implies that nonlocal interactions are yet another mechanism that may mediate dot–dot interaction (even in the isotropic case; the interactions are expected to be yet stronger in the anisotropic case). Given the computational advances, these many body interaction effects can be accounted for easily (and indeed have been implicitly done in several numerical works). To the best of the authors’ knowledge, however, a systematic study is not yet available.

Frequently, quantum dots are assumed to have identical material properties as the barrier. Computationally, there is no difficulty in accounting for the modulus mismatch (and indeed is routinely done in numerical simulations). The question, however, remains as to what truly are the material properties of the quantum dot that is often an alloy and under strain. Arguments may be advanced from both points of view. Indeed, some works have justified using identical material properties based on Keyes scaling relation [90–92]. Further, in a binary or ternary mixture, phases are not often uniformly intermixed [191]. For example, InGaN quantum dots one often sees a preferential phase segregation into InN [193]. How uniform is the mixing and hence the strain state in quantum dots? These aforementioned issues certainly could benefit from more detailed experimentation and theoretical work.

Although we have hardly touched on the strain-band structure coupling in this chapter, we mention here that several works have studied the viability and applicability of various approaches to take into account strain-band structure coupling. An oft-quoted work is that due to Pikus and Bir [194]. Other works have extended and modified this in various fashions, which we do not discuss here (e.g., Ref. [195] and the eight-band model, [196–197]). The particular reference that we would like to cite is due to Zhang [198] who presents formalism for taking into account inhomogeneous strain. This is an important advance however, largely predicated on the strain potential (in the quantum mechanical Hamiltonian) being local, that is the deformation potential at a point solely on the strain at that point. As acknowledged by Zhang himself (which in turn was communicated to him by C. Herring), the true strain potential is nonlocal. The implications of altering his formulation to reflect this fact remains unresolved. Modification of the Zhang Hamiltonian [198] along with possibly *ab initio* computation to investigate this issue is an interesting research avenue.

ACKNOWLEDGMENTS

The second author acknowledges fruitful collaborations with Xinyuan Zhang, Dr. Surya Ganti and Dr. Azar Alizadeh. We are grateful to the researchers who kindly provided us with permissions and original pictures from their research for inclusion in this article.

REFERENCES

1. Y. Arakawa, *IEEE, J. Sel. Top. Quantum Electron.* 8, 823 (2002).
2. S. Nakamura, S. Pearton, and G. Fasol, “The Blue Laser Diode: The Complete Story.” Springer, Berlin, 2000.
3. D. G. Deppe and D. L. Huffaker, *Appl. Phys. Lett.* 77, 3325 (2000).

4. Bhattacharya and Ghosh.
5. T. Lundstrom, W. Schoenfeld, H. Lee, and P. M. Petroff, *Science* 286, 2312 (1999).
6. Y. Chye, M. E. White, E. Johnston-Halperin, B. D. Gerardot, D. D. Awschalom, and P. M. Petroff, *Phys. Rev. B* 66, 201301 (2002).
7. P. M. Petroff, *Top. Appl. Phys.* 90, 1 (2003).
8. P. Alivisatos, *TOPS* 40, 86 (2000).
9. P. Bhattacharya, A. D. Stiff-Roberts, S. Krishna, and S. Kennerly, *Int. J. High Speed Electron. and Syst.* 12, 969 (2002).
10. J. Tersoff, C. Teichert, and M. G. Lagally, *Phys. Rev. Lett.* 76, 1675 (1996).
11. D. Bimberg, *Semiconductors* 33, 951 (1999).
12. D. Bimberg, M. Grundmann, and N. N. Ledentsov, "Quantum Dot Heterostructures." Wiley, New York, 1998.
13. L. B. Freund and H. T. Johnson, *J. Mech. Phys. Solids* 49, 1925 (2001).
14. H. T. Johnson and L. B. Freund, *Int. J. Solids. Struct.* 38, 1045 (2001).
15. E. P. O'Reilly, *Semicond. Sci. Technol.* 4, 121 (1989).
16. E. P. O'Reilly and A. R. Adams, *IEEE J. Quantum Electron.* 30, 366 (1994).
17. A. Alizadeh, P. Sharma, S. Ganti, S. F. LeBoeuf, and L. Tsakalagos, *J. Appl. Phys.* 95, 8199 (2004).
18. J. O. Winter, T. Y. Liu, B. A. Korgel, and C. E. Schmidt, *Adv. Mater.* 3, 1673 (2001).
19. J. C. Chen, A. M. Chang, and M. R. Melloch, *Phys. Rev. Lett.* 92, 176801 (2004).
20. I. L. Medintz, A. R. Clapp, H. Mattoussi, E. R. Goldman, B. Fisher, and J. M. Mauro, *Nat. Mater.* 2, 630 (2003).
21. P. Harrison, "Quantum Wells, Wires and Dots: Theoretical and Computational Physics." Wiley, 2000.
22. J. Singh, "Physics of Semiconductors and Their Heterostructures." McGraw-Hill College, 1992.
23. M. Yang, J. C. Strum, and J. Provost, *Phys. Rev. B* 56, 1973 (1997).
24. M. S. Miller, J.-O. Malm, M. E. Pistol, S. Jeppesen, B. Kowalski, K. Georgsson, and L. Samuelson, *J. Appl. Phys.* 80, 3360 (1996).
25. G. S. Solomon, J. A. Trezza, J. A. Marshall, and J. A. Harris, Jr., *Phys. Rev. Lett.* 76, 952 (1996).
26. Q. Xie, A. Madhukar, P. Chen, and N. P. Kobayashi, *Phys. Rev. Lett.* 75, 2542 (1995).
27. M. Grundmann, O. Stier, and D. Bimberg, *Phys. Rev. B* 52, 11969 (1995).
28. M. Moreno, A. Trampert, B. Jenichen, L. Daweritz, and K. H. Ploog, *J. Appl. Phys.* 92, 4672 (2002).
29. A. Lenz, R. Timm, H. Eisele, Ch. Hennig, S. K. Becker, R. L. Sellin, U. W. Pohl, D. Bimberg, and M. Dahne, *Appl. Phys. Lett.* 81, 5150 (2002).
30. J. D. Eshelby, *Proc. R. Soc. London, Ser. A* 241, 376 (1957).
31. J. D. Eshelby, *Proc. R. Soc. London, Ser. A* 252, 561 (1959).
32. J. D. Eshelby, in "Progress in Solid Mechanics 2" (I. N. Sneddon and R. Hill, Eds.). North Holland, Amsterdam, 1961.
33. S. Nemat-Nasser and M. Hori, "Micromechanics: Overall Properties of Heterogeneous Solids." Elsevier, 1999.
34. L. D. Landau and E. M. Lifshitz, "The Classical Theory of Fields." Butterworth-Heinemann, 1980, Vol. 2.
35. T. Mura, "Micromechanics of Defects in Solids," 2nd Edn.
36. O. D. Kellogg, "Foundations of Potential Theory." Dover, New York, 1954.
37. D. H. Armitage and S. J. Gardiner, *Classical Potential Theory*. Springer, 2000.
38. A. Blech and E. S. Meieran, *J. Appl. Phys.* 38, 2913 (1967).
39. S. M. Hu, *J. Appl. Phys.* 50, 4661 (1979).
40. A. Fischer and H. Richter, *Appl. Phys. Lett.* 61, 2656 (1992).
41. P. A. Kirkby, P. R. Selway, and L. D. Westbrook, *J. Appl. Phys.* 50, 4567 (1979).
42. S. Christiansen, M. Albrecht, H. P. Strunk, and H. J. Maier, *Appl. Phys. Lett.* 64, 3617 (1994).
43. J. Massies and N. Grandjean, *Phys. Rev. Lett.* 71, 1411 (1993).
44. F. Glas, *J. Appl. Phys.* 70, 3556 (1991).
45. J. Y. Marzin and G. Bastard, *Solid State Commun.* 92, 437 (1994).
46. C. Priester, I. Lefebvre, G. Allan, and M. Lannoo, in "MRS Symposia Proceedings No. 317."
47. S. Christiansen, M. Albrecht, H. P. Strunk, and H. J. Maier, *Appl. Phys. Lett.* 64, 3617 (1994).
48. M. Grundmann, O. Stier, and D. Bimberg, *Phys. Rev. B* 52, 11969 (1995).
49. J. R. Downes, D. A. Faux, and E. P. O'Reilly, *J. Appl. Phys.* 81, 6700 (1997).
50. Y. P. Chiu, *J. Appl. Mech.* 45, 302 (1978).
51. T. Bennabas, P. Francios, Y. Androussi, and A. Lefebvre, *J. Appl. Phys.* 80, 2763 (1996).
52. G. S. Pearson and D. A. Faux, *J. Appl. Phys.* 88, 730 (2000).
53. P. W. Fry, I. E. Itskevich, D. J. Mowbray, M. S. Skolnick, J. A. Barker, E. P. O'Reilly, L. R. Wilson, I. A. Larkin, P. A. Maksym, M. Hopkinson, M. Al-Khafiji, J. P. R. David, A. G. Cullis, G. Hill, and J. C. Clark, *Phys. Rev. Lett.* 84, 733 (2000).
54. J. H. Davies, *J. Appl. Phys.* 84, 1358 (1998).
55. K. Nishi, A. A. Yamaguchi, J. Ahopelto, A. Usui, and H. Sakaki, *J. Appl. Phys.* 76, 7437 (1994).
56. C. Pryor, M. E. Pistol, and L. Samuelson, *Phys. Rev. B* 56, 10404 (1997).
57. C. Pryor, *Phys. Rev. B* 57, 7190 (1998).
58. C. Pryor, J. Kim, L. W. Wang, A. J. Williamson, and A. Zunger, *J. Appl. Phys.* 83, 2548 (1998).
59. M. Tadić, F. M. Peeters, K. L. Janssens, M. Korkusinski, and P. Hawrylak, *J. Appl. Phys.* 92, 5819 (2002).
60. M. Korkusinski and P. Hawrylak, *Phys. Rev. B* 63, 195311 (2001).
61. H. Shin, W. Lee, and Y. H. Yoo, *J. Phys.* 15, 3689 (2003).
62. S. H. Bellaiche, L. Wei, and A. Zunger, *Phys. Rev. B* 54, 18568 (1996).

63. J. Bernard and A. Zunger, *Appl. Phys. Lett.* 65, 165 (1994).
64. M. Cusack, P. Briddon, and M. Jaros, *Phys. Rev. B* 54, R2300 (1996).
65. H. Jiang and J. Singh, *Phys. Rev. B* 56, 4696 (1997).
66. P. N. Keating, *Phys. Rev.* 145, 637 (1966).
67. R. M. Martin, *Phys. Rev. B* 1, 4005 (1970).
68. F. H. Stillinger and T. A. Weber, *Phys. Rev. B* 31, 5262 (1985).
69. W. Yu and A. Madhukar, *Phys. Rev. Lett.* 79, 905 (1997).
70. W. Yu and A. Madhukar, *Phys. Rev. Lett.* 79, 4939 (1997).
71. M. A. Makeev and A. Madhukar, *Phys. Rev. B* 67, 073201 (2003).
72. M. A. Migliorato, A. G. Cullis, M. Fearn, and J. H. Jefferson, *Phys. Rev. B* 65, 115316 (2002).
73. O. Brandt, K. Ploog, R. Bierwolf, and M. Hosenstein, *Phys. Rev. Lett.* 68, 1339 (1992).
74. J. R. Downes and D. A. Faux, *J. Appl. Phys.* 77, 2444 (1995).
75. D. A. Faux, S. G. Howells, U. Bangert, and A. J. Harvey, *Appl. Phys. Lett.* 64, 1271 (1994).
76. E. Kapon, M. Walther, J. Christen, M. Grundmann, C. Caneau, D. M. Hwang, E. Colas, R. Bhat, G. H. Song, and D. M. Bimberg, *Superlattices Microstruct.* 12, 491 (1992).
77. T. Arakawa, S. Tsukamoto, Y. Nagamune, M. Nishioka, J.-H. Lee, and Y. Arakawa, *Jpn. J. Appl. Phys.* 32, L1377 (1993).
78. N. Usami, T. Mine, S. Fukatsu, and Y. Shiraki, *Appl. Phys. Lett.* 64, 1126 (1994).
79. H. Weman and E. Kapon, EPFL.
80. T. J. Gosling and J. R. Willis, *J. Appl. Phys.* 77, 5601 (1995).
81. T. Yamauchi, Y. Arakawa, and J. N. Schulman, *Surf. Sci.* 267, 291 (1992).
82. Y. Arakawa, *IEEE Trans. Fundamentals* E75-A, 20 (1992).
83. T. Yamauchi, T. Takahashi, J. N. Schulman, and Y. Arakawa, *IEEE J. Quantum Electron.* QE-29, 2109 (1993).
84. T. J. Gosling and L. B. Freund, *Acta. Mater.* 44, 1 (1996).
85. G. Bilalbegovic, *Phys. Rev. B* 58, 15412 (1998).
86. I. A. Ovid'ko, *Phys. Rev. Lett.* 88, 046103 (2002).
87. M. E. Sherwin, T. J. Dummond, and D. J. Srolovitz, *J. Appl. Phys.* 69, 717 (1991).
88. D. A. Faux, J. R. Downes, and E. P. O'Reilly, *J. Appl. Phys.* 80, 2515 (1996).
89. K. Nishi, A. A. Yamaguchi, J. Ahopelto, A. Usui, and H. Sakaki, *J. Appl. Phys.* 76, 7437 (1994).
90. J. R. Downes, D. A. Faux, and E. P. O'Reilly, *J. Appl. Phys.* 82, 3754 (1997).
91. R. W. Keyes, *J. Appl. Phys.* 33, 3371 (1962).
92. A. D. Prins and D. J. Dunstan, *Philos. Mag. Lett.* 58, 37 (1988).
93. A. D. Andreev, J. R. Downes, D. A. Faux, and E. P. O'Reilly, *J. Appl. Phys.* 86, 297 (1999).
94. A. E. Romanov, P. M. Petroff, and J. S. Speck, *Appl. Phys. Lett.* 74, 2280 (1999).
95. H. Lee, J. A. Johnson, J. S. Speck, and P. M. Petroff, *J. Vac. Sci. Technol.* 18, 2193 (2000).
96. R. D. Mindlin and D. H. Cheng, *J. Appl. Phys.* 21, 926 (1950).
97. R. D. Mindlin, and D. H. Cheng, *J. Appl. Phys.* 21, 931 (1950).
98. J. N. Goodier, *Philos. Mag.* 23, 1017 (1937).
99. S. P. Timoshenko and J. N. Goodier, "Theory of Elasticity," 3rd Edn. McGraw-Hill, New York, 1970.
100. J. H. Davies, *J. Appl. Mech.* 70, 655 (2003).
101. R. D. Mindlin, *Midwestern Conf. Solid Mech.* 56 (1953).
102. K. Seo and T. Mura, *J. Appl. Mech.* 46, 568 (1979).
103. F. Glas, *J. Appl. Phys.* 90, 3232 (2001).
104. F. Glas, *Appl. Surf. Sci.* 188, 9 (2002).
105. F. Glas, *Philos. Mag. A* 82, 2591 (2002).
106. R. I. Barabash and M. A. Krivoglaz, *Fiz. Tverd. Tela* (Leningrad) 29, 3081 (1987).
107. A. E. Romanov, G. E. Beltz, W. T. Fischer, P. M. Petroff, and J. S. Speck, *J. Appl. Phys.* 89, 4523 (2001).
108. D. A. Faux and J. Haigh, *J. Phys.* 2, 10289 (1990).
109. P. H. Dederichs and G. Leibfried, *Phys. Rev.* 188, 1175 (1969).
110. J. W. Flocken and J. R. Hardy, *Phys. Rev. B* 1, 2447 (1970).
111. R. A. Masamura and G. Sines, *J. Appl. Phys.* 41, 3930 (1970).
112. P. H. Dederichs and J. Pollman, *Z. Phys.* 255, 315 (1972).
113. T. Mura and N. Kinoshita, *Phys. Status Solidi B* 47, 607 (1971).
114. I. M. Lifshits and L. N. Rosentsverg, *Zh. Eks. Teor. Fiz* 17, 9 (1947); [*Sov. Phys. JETP*].
115. D. A. Faux and G. S. Pearson, *Phys. Rev. B* 62, R4798 (2000).
116. E. Pan and F. G. Yuan, *Int. J. Solid Struct.* 37, 5329 (2000).
117. D. M. Barnett and J. Lothe, *Phys. Norv.* 8, 13 (1975).
118. J. R. Barber and F. A. Sturla, *J. Mech. Phys. Solids* 40, 17 (1992).
119. T. C. T. Ting, "Anisotropic Elasticity." Oxford University Press, Oxford, UK, 1996.
120. K. C. Wu, *J. Elast.* 51, 213 (1998).
121. Y. C. Pan and T. W. Chou, *Int. J. Eng. Sci.* 17, 545 (1979).
122. Q. X. Pei, C. Lu, and Y. Y. Wang, *J. Appl. Phys.* 93, 1487 (2003).
123. S. W. Ellaway and D. A. Faux, *J. Appl. Phys.* 92, 3027 (2002).
124. M. J. Mehl, J. E. Osburn, D. A. Papaconstantopoulos, and B. M. Klein, *Phys. Rev. B* 41, 10311 (1990).
125. M. J. Mehl, J. E. Osburn, D. A. Papaconstantopoulos, and B. M. Klein, *Phys. Rev. B* 42, 5362 (1990).
126. M. J. Mehl, *Phys. Rev. B* 47, 2493 (1993).
127. M. Ichimura, *Phys. Status Solidi A* 153, 431 (1996).

128. S. W. Ellaway and D. A. Faux, *Phys. Status Solidi B* 235, 437 (2003).
129. M. D. Frogley, J. L. Sly, and D. J. Dunstan, *Phys. Rev. B* 58, 12579 (1998).
130. M. D. Frogley, J. R. Downes, and D. J. Dunstan, *Phys. Rev. B* 62, 13612 (2000).
131. S. P. Lepkowski and J. A. Majewski, *Acta Phys. Pol. A* 105, 559 (2004).
132. S. P. Lepkowski and J. A. Majewski, *Solid State Commun.* 131, 763 (2004).
133. B. W. Kim, *J. Appl. Phys.* 89, 1197 (2001).
134. S. Sanguinetti, M. Gurioli, E. Grilli, M. Guzzi, and M. Henini, *Thin Solid Films* 380, 198 (2000).
135. A. Patane, A. Levin, A. Polimeni, F. Schindler, P. C. Main, L. Eaves, and M. Henini, *Appl. Phys. Lett.* 77, 2979 (2000).
136. J. F. Nye, "Physical Properties of Crystals." Clarendon, Oxford, 1985.
137. B. Jogai, *J. Appl. Phys.* 90, 699 (2001).
138. E. Pan, *J. Appl. Phys.* 91, 3785 (2002).
139. E. Pan, *Proc. R. Soc. London, Ser. A* 458, 181 (2002).
140. D. M. Barnett and J. Lothe, *Phys. Norv.* 8, 13 (1975).
141. E. Pan, *J. Appl. Phys.* 91, 6379 (2002).
142. P. Sharma and S. Ganti, *Phys. Status Solidi B* 234, R10 (2002).
143. A. Alizadeh, P. Sharma, S. Ganti, S. LeBoeuf, and L. Tsakalagos, *J. Appl. Phys.* 95, 8199 (2004).
144. P. Sharma and S. Ganti, *J. Appl. Mech.* 71, 663 (2004).
145. R. E. Miller and V. B. Shenoy, *Nanotechnology* 11, 139 (2000).
146. R. C. Cammarata, K. Sieradzki, and F. Spaepen, *J. Appl. Phys.* 87, 1227 (2000).
147. R. Kukta, A. Peralta, and D. Kouris, *J. Appl. Mech.* 69, 443 (2002).
148. D. A. Kouris, E. Tsuchida, and T. Mura, *J. Appl. Mech.* 53, 724 (1986).
149. M. E. Gurtin and A. I. Murdoch, *Arch. Ration. Mech. Anal.* 59, 389 (1978).
150. Murdoch.
151. M. E. Gurtin, J. Weissmuller, and F. Larche, *Philos. Mag. A* 78, 1093 (1998).
152. H. Ibach, *Surf. Sci. Rep.* 29, 193 (1997).
153. P. Sharma and S. Ganti, *Philos. Mag. Lett.* 83, 745 (2003).
154. P. Sharma, S. Ganti, and N. Bhate, *Appl. Phys. Lett.* 82, 535 (2003).
155. P. Sharma and S. Ganti, *J. Appl. Mech.* 71, 663 (2004).
156. X. Peng, S. Ganti, P. Sharma, A. Alizadeh, S. Nayak, and S. Kumar, 2005, in review.
157. C. Eringen, "Nonlocal Continuum Field Theories." Springer, New York, 2002.
158. H. Kleinert, "Gauge Fields in Condensed Matter." World Scientific, 1989, Vol. 2.
159. B. Delley and E. F. Steigmeier, *Appl. Phys. Lett.* 67, 2370 (1995).
160. X. Zhang and P. Sharma, *Int. J. Solids Struct.* 42, 3833 (2005).
161. D. P. DiVincenzo, *Phys. Rev. B* 34, 5450 (1986).
162. C. Q. Ru, *Acta. Mech.* 160, 219 (2003).
163. J. Y. Li and M. L. Dunn, *Philos. Mag. A* 77, 1341 (1998).
164. E. Pan and B. Yang, *J. Appl. Phys.* 93, 2435 (2003).
165. G. J. Rodin, *J. Mech. Phys. Solids* 44, 1977 (1996).
166. H. Nozaki and M. Taya, *J. Appl. Mech.* 68, 441 (2001).
167. R. Furuhashi, J. H. Huang, and T. Mura, *J. Appl. Mech.* 59, 783 (1992).
168. C. Q. Ru and P. Schiavone, *Proc. R. Soc. London A* 453, 2551 (1997).
169. Z. Zhong and S. A. Meguid, *J. Appl. Mech.* 63, 877 (1996).
170. J. Qu, *Mech. Mater.* 14, 269 (1993).
171. J. Qu, *J. Appl. Mech.* 60, 1048 (1993).
172. L. J. Walpole, *Math. Proc. Cambridge* 83, 495 (1978).
173. H. A. Luo and G. J. Weng, *Mech. Mater.* 8, 77 (1989).
174. M. Cherkaoui, H. Sabar, and M. Berveiller, *J. Eng. Mater.* 116, 274 (1994).
175. G. P. Sendeckyj, Ph.D. Dissertation, Northwestern University, Evanston, 1967.
176. Z. A. Moschovidis, Ph.D. Dissertation, Northwestern University, 1975.
177. G. J. Rodin and Y.-L. Hwang, *Int. J. Solids Struct.* 27, 145 (1991).
178. R. J. Asaro and D. M. Barnett, *J. Mech. Phys. Solids* 23, 77 (1975).
179. T. Mura and N. Kinoshita, *Phys. Status Solidi A* 48, 447 (1978).
180. M. Rahman, *J. Appl. Mech.* 69, 593 (2002).
181. A. C. Eringen, "Microcontinuum Field Theories I: Foundations and Solids." Springer, New York, 1999.
182. Z. Q. Cheng and L. H. Le, *Int. J. Eng. Sci.* 33, 389 (1995).
183. Z. Q. Cheng and L. H. Le, *Int. J. Eng. Sci.* 35, 659 (1997).
184. P. Sharma and A. Dasgupta, *Phys. Rev. B* 66, 224110 (2002).
185. K. Markov and L. Preziosi, "Heterogeneous Media: Micromechanics Modeling Methods and Simulations." Birkhauser, Switzerland, 2000.
186. G. J. Weng, M. Taya, and H. Abe, (Eds.), "Micromechanics and Inhomogeneity: The Toshio Mura Anniversary Volume." Springer, 1990.
187. B. A. Bilby, K. J. Miller, and J. R. Willis, IUTAM/IFC/ICM Symposium on Fundamentals of Deformation and Fracture, Sheffield, England, Eshelby Memorial Symposium. Cambridge University Press, Cambridge, 1984.
188. T. Mura, H. M. Shodja, and Y. Hirose, *Appl. Mech. Rev.* 49, S118 (1996).
189. T. Mura, *Mater. Sci. Eng. A* 285, 224 (2000).
190. Y. Kikuchi, H. Sugii, and K. Shintani, *J. Appl. Phys.* 89, 1191 (2001).

191. J. Stangl, V. Holy, and G. Bauer, *Rev. Mod. Phys.* 76, 725 (2004).
192. W. J. Drugan and J. R. Willis, *J. Mech. Phys. Solids* 44, 497 (1996).
193. A. Alizadeh, (Personal communication, 2005).
194. G. E. Pikus and G. L. Bir, *Sov. Phys. Solid State* 1, 1502 (1960).
195. G. E. Pikus and G. L. Bir, "Symmetry and Strain Induced Effects in Semiconductors." Wiley, New York, 1974.
196. T. B. Bahder, *Phys. Rev. B* 41, 11992 (1989).
197. T. B. Bahder, *Phys. Rev. B* 46, 9913 (1992).
198. Y. Zhang, *Phys. Rev. B* 49, 14352 (1994).